iScience

CellPress
OPEN ACCESS

Article

CD168^{+} macrophages promote hepatocellular carcinoma tumor stemness and progression through *TOP2A*/β-catenin/*YAP1* axis

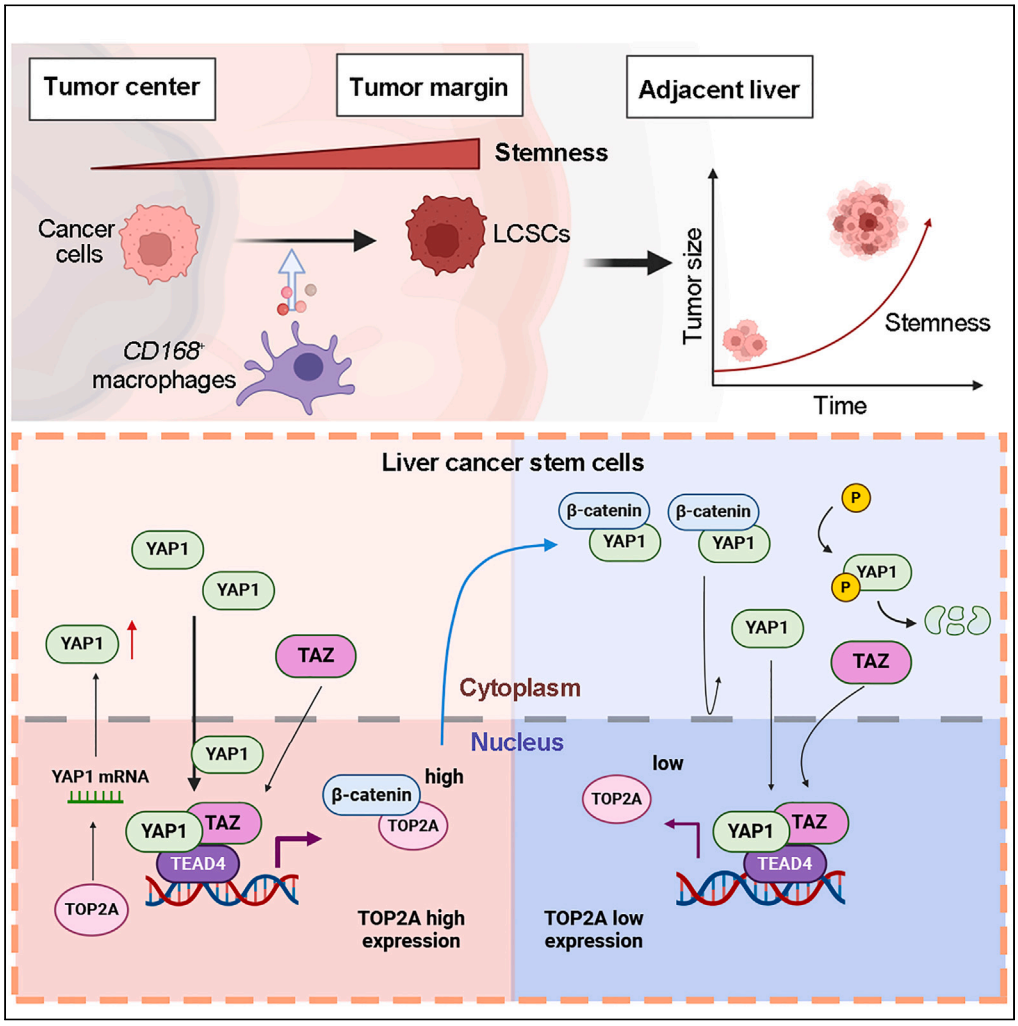

Hai-Chao Zhao, Chang-Zhou Chen, Yan-Zhang Tian, ..., Yan-Jun Li, Jie-Feng He, Hao-Liang Zhao

hejiefeng2008@163.com (J.-F.H.)
haoliangzhao@hotmail.com (H.-L.Z.)

Highlights

Liver cancer stem cells enriched at tumor margins are identified by scRNA-seq

CD168^{+} macrophages drive liver cancer stem cells generation via cell-cell interactions

TOP2A plays a crucial role in enhancing the stem-like properties of hepatic cancer cells

TOP2A promotes stemness by competitively binding to β-catenin and disassociating YAP1

Zhao et al., iScience *26*, 106862
June 16, 2023
https://doi.org/10.1016/j.isci.2023.106862

iScience

CellPress
OPEN ACCESS

Article

CD168^{+} macrophages promote hepatocellular carcinoma tumor stemness and progression through *TOP2A*/β-catenin/*YAP1* axis

Hai-Chao Zhao,[1,2,4] Chang-Zhou Chen,[2,4] Yan-Zhang Tian,[3,4] Huang-Qin Song,[1] Xiao-Xiao Wang,[1] Yan-Jun Li,[3] Jie-Feng He,[1,3,*] and Hao-Liang Zhao[1,3,5,*]

SUMMARY

Liver cancer stem-like cells (LCSCs) are the main cause of heterogeneity and poor prognosis in hepatocellular carcinoma (HCC). In this study, we aimed to explore the origin of LCSCs and the role of the TOP2A/β-catenin/YAP1 axis in tumor stemness and progression. Using single-cell RNA-seq analysis, we identified *TOP2A*$^{+}$*CENPF*$^{+}$ LCSCs, which were mainly regulated by *CD168*$^{+}$ M2-like macrophages. Furthermore, spatial location analysis and fluorescent staining confirmed that LCSCs were enriched at tumor margins, constituting the spatial heterogeneity of HCC. Mechanistically, TOP2A competitively binds to β-catenin, leading to disassociation of β-catenin from YAP1, promoting HCC stemness and overgrowth. Our study provides valuable insights into the spatial transcriptome heterogeneity of the HCC microenvironment and the critical role of TOP2A/β-catenin/YAP1 axis in HCC stemness and progression.

INTRODUCTION

Liver cancer is the fourth cause of cancer-related deaths in the world, and the number of deaths is increasing year by year.[1] Hepatocellular carcinoma (HCC) is the main type of liver cancer, accounting for 75–85%.[2] Tumor heterogeneity leads to insufficient tumor cell genetic characteristics and microenvironmental information obtained from a single biopsy.[3] Different sensitivity of cancer cells to the drug may lead to the failure of targeted therapy or immunotherapy.[4]

The heterogeneity of HCC makes it quite difficult to identify genetic variants based on bulk mRNA sequencing.[5] The overall progress in identifying operable diagnostic markers and therapeutic targets is still largely hindered because of the limitations of batch analysis techniques in capturing intratumoral heterogeneity. Single-cell transcriptomics sequencing technology can greatly make up for the shortcomings of traditional bulk RNA-seq and has become a new method to reveal the heterogeneity of tumor transcriptomics in recent years.[6–8] The spatial heterogeneity of solid tumors is a question worth exploring. Although the spatial transcriptome can explore the genetic information of tumor cells in space,[9] it is restricted by the size of the exploration space. At present, some studies have combined single-cell transcriptome and spatial transcriptome technologies, which can better describe the spatial changes of tumors.[10,11] Spatially, the interaction among tumor subgroup and the effect of tumor immune microenvironment (TIME) on cancer cells have enormous implications for tumor evolution.

The HCC cell stemness is the main culprit of tumor heterogeneity.[12] Owing to self-renewal and unlimited proliferation, this small group of liver cancer stem-like cells (LCSCs) act as the driver of cancer, greatly promoting the rapid progress of HCC. There have been studies on the generation of CSCs, such as abnormal activation of pathways[13] or mutations of TP53.[14] However, in addition to the changes in stem cells themselves, their environment also plays a vital role in promoting the stemness of cancer cells. At present, scholars have explored the role of CSCs in disease progression through single-cell sequencing technology.[15,16] The polyclonal proliferation of cancer cells and the killing effect of immune cells led to the Darwinian selection of cancer cells, leaving more malignant cancer stem cells (CSCs).[17]

[1]Third Hospital of Shanxi Medical University, Shanxi Academy of Medical Sciences, Taiyuan 030032, China

[2]Department of Liver Surgery and Transplantation, Liver Cancer Institute, Zhongshan Hospital, Fudan University, Shanghai 200032, China

[3]Shanxi Bethune Hospital, Shanxi Academy of Medical Sciences, Taiyuan 030032, China

[4]These author contributed equally

[5]Lead contact

*Correspondence: hejiefeng2008@163.com (J.-F.H.), haoliangzhao@hotmail.com (H.-L.Z.)

https://doi.org/10.1016/j.isci.2023.106862

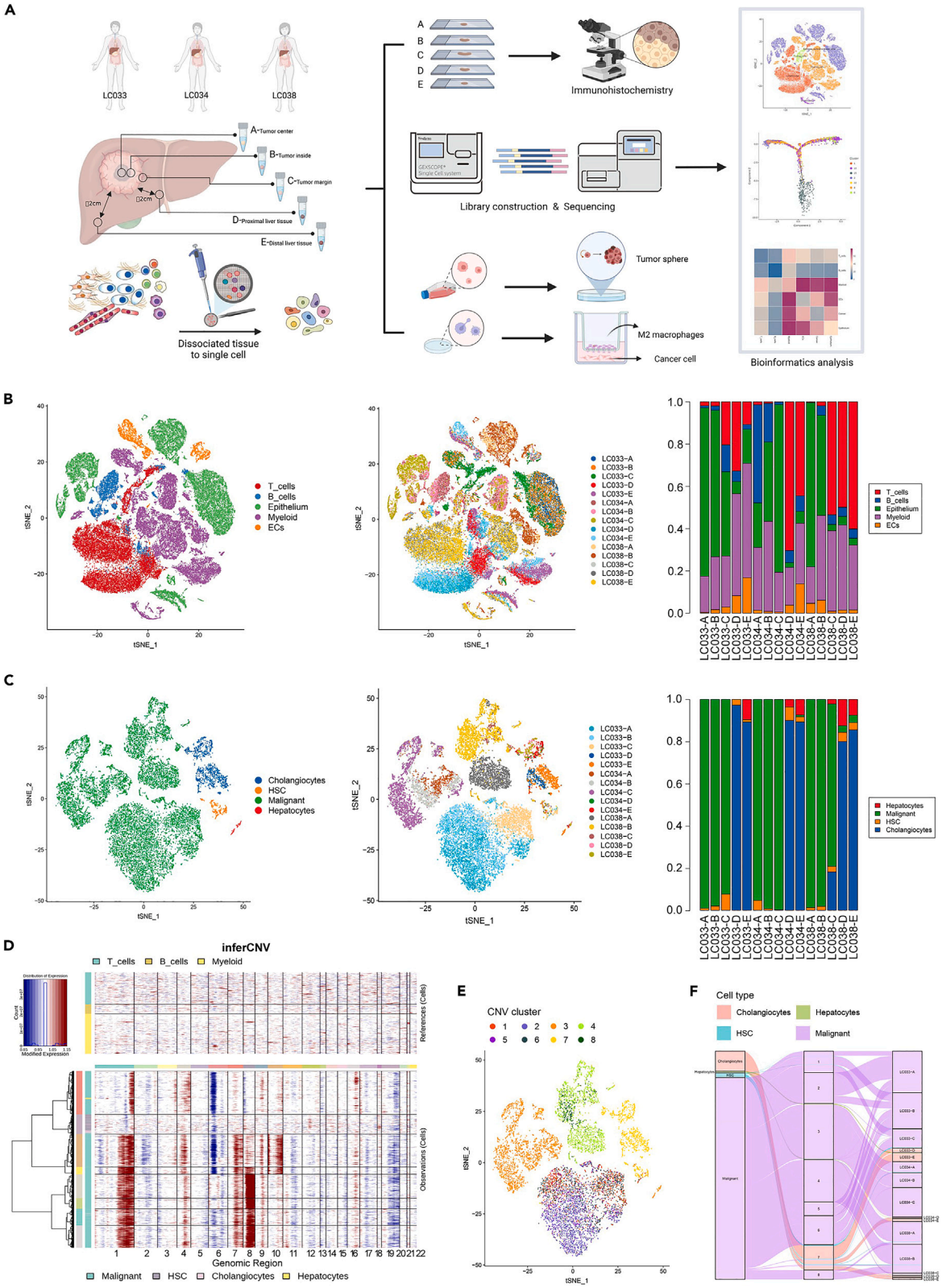
A
LC033
LC034
LC038
A-Tumor center
B-Tumor inside
C-Tumor margin
D-Proximal liver tissue
E-Distal liver tissue
≥2cm
≥2cm
Dissociated tissue
to single cell
A
B
C
D
E
Immunohistochemistry
Library construction & Sequencing
Tumor sphere
M2 macrophages
Cancer cell
Bioinformatics analysis
B
tSNE_1
tSNE_2
T_cells
B_cells
Epithelium
Myeloid
ECs
LC033-A
LC033-B
LC033-C
LC033-D
LC033-E
LC034-A
LC034-B
LC034-C
LC034-D
LC034-E
LC038-A
LC038-B
LC038-C
LC038-D
LC038-E
C
Cholangiocytes
HSC
Malignant
Hepatocytes
D
inferCNV
T_cells
B_cells
Myeloid
References (Cells)
Observations (Cells)
Genomic Region
Malignant
HSC
Cholangiocytes
Hepatocytes
E
CNV cluster
F
Cell type
Cholangiocytes
Hepatocytes
HSC
Malignant

Figure 1. scRNA-seq profiling of the HCC tumor environments

(A) Schematic representation showing the collection and processing of fresh samples from primary HCC tumors and ANT for scRNA-seq.

(B) All cell clusters profiled in this study. Left, *t*-SNE plot showing the annotation and color codes for cell types in the HCC ecosystem. Middle, *t*-SNE plot showing cell origins by color. Each color indicates one sample. Right, Histogram indicating the proportion of different cell types in the 15 samples.

(C) Epithelial cells clusters in HCC and ANT. Left, t-SNE plot of 4 epithelial cell subtypes identified from 3,717 epithelial cells. Middle, t-SNE plot of Epithelial Cells from 15 samples (indicated by colors). Right, Histogram indicating the proportion of different epithelial cell types in the 15 samples.

(D) Chromosomal landscape of inferred large-scale CNVs distinguishing malignant cells from epithelial cells. The CNV of immune cells are plotted in the top heatmap, and malignant cells are plotted in the bottom heatmap. Amplifications (red) or deletions (blue) were inferred by averaging expression over 100-gene stretches on the indicated chromosomes.

(E) t-SNE plot of CNV clustering of epithelial cells.

(F) Sankey diagram showing cell types, CNV clusters and sample sources in Epithelial Cells. ANT, adjacent non-tumor tissue.

Here, we use the single-cell transcriptome method to comprehensively describe the HCC landscape with 82,030 cells separated from 15 samples. We analyzed the heterogeneity of cancer cells and found spatial characteristics of LCSCs. In addition, based on the spatial distribution, we explored the causes of LCSCs formation and the main driver genes that maintain the stemness of HCC cells. Therefore, our results will improve the understanding of the distribution and formation of LCSCs.

RESULTS

Single-cell expression atlas and cell types of the TME in HCC

We obtained scRNA-seq profiles of 15 samples from 3 HCC patients (Table S1 for clinical information; Figure S1 for imaging), and a total of 82,030 cells were collected for analysis (Figure 1A). After quality control and double-cells removal (Figure S2A, see STAR Methods), 68,448 cells were divided into 42 clusters (Figure S2B). We have drawn a comprehensive multi-site single-cell transcriptome atlas of HCC solid tumors, including T lymphocytes, B lymphocytes, epithelial cells, myeloid cells, and endothelial cells (Figure 1B, andTable S3). Correspondingly, typical cell markers were used to identify cell types, such as *CD3D*, *CD2*, and *CD3E* for T cells, *MZB1*, *CD79A*, *IGHG1*, *JCHAIN* and *MS4A1* for B cells, *APOA2*, *HP*, *ALB* and *APOA1* for epithelial cells, and *CD68* for myeloid cells (Figures S3 and S4).

Subsequently, epithelial cells are divided into 18 subclusters after dimensionality reduction (Figure S5A). According to the cell markers (Figures S5B, S5C and S6), they are mainly classified into malignant cells, cholangiocytes, hepatic stellate cells (HSCs), and hepatocytes (Figure 1C). According to the source of the sample, we observed that cholangiocytes, HSCs and hepatocyte clusters showed a mixture of three patients (Figures 1C and S5D). The malignant cells were divided into three groups and they were independent of each other (Figures 1C and S5D), which shows heterogeneity among patients. In addition, cluster annotation was performed according to HBV infection (Figure S5E).

Because malignant cells do not have specific markers, it is difficult to define them with cell markers. We identified cancer cells based on sample heterogeneity and chromosome copy number variation (CNV). We calculated the large-scale CNV of each cell based on the average expression pattern of the genome interval,[18] and found that the CNV level of malignant cells was significantly higher than immune cells as control (Figure 1D). Epithelial cell clusters were divided into CNV1-8 groups according to the CNV levels (Figure 1E). The CNV of non-malignant cells was relatively single, and most of them belong to the CNV 7 group; however, cancer cells showed large differences in CNV, covering CNV1-6 and 8 groups (Figures 1E and 1F). After removing the cancer cells, HSC was found mainly in points A, B and C (Figure S5F), which may be related to the specific tumor promotion effect played by HSC activation.[19] In summary, inter-tumor heterogeneity was described and liver cancer cells were found in the epithelium via CNV.

Tumor heterogeneity and stemness of cancer cells

Cancer cells were divided into 22 subclusters and annotated according to sample origin and CNV (Figure 2A). Not only different patients did not share the same cancer cell cluster, but cancer cells at different points (tumor center A, middle B, margin C) exhibited different transcriptomic characteristics. In order to explore the spatial distribution of cancer cells, we displayed clusters according to sampling points (Figure 2A). We found that there is a spatial distribution pattern of cancer cells (gradually increasing or decreasing) from the center of the tumor to the margin (Figure 2B). In addition, most cancer cells were in a certain proportion of cycle, while Cluster 12, 15, 17, and 20 were mostly in the G2/M phase (Figure 2C),

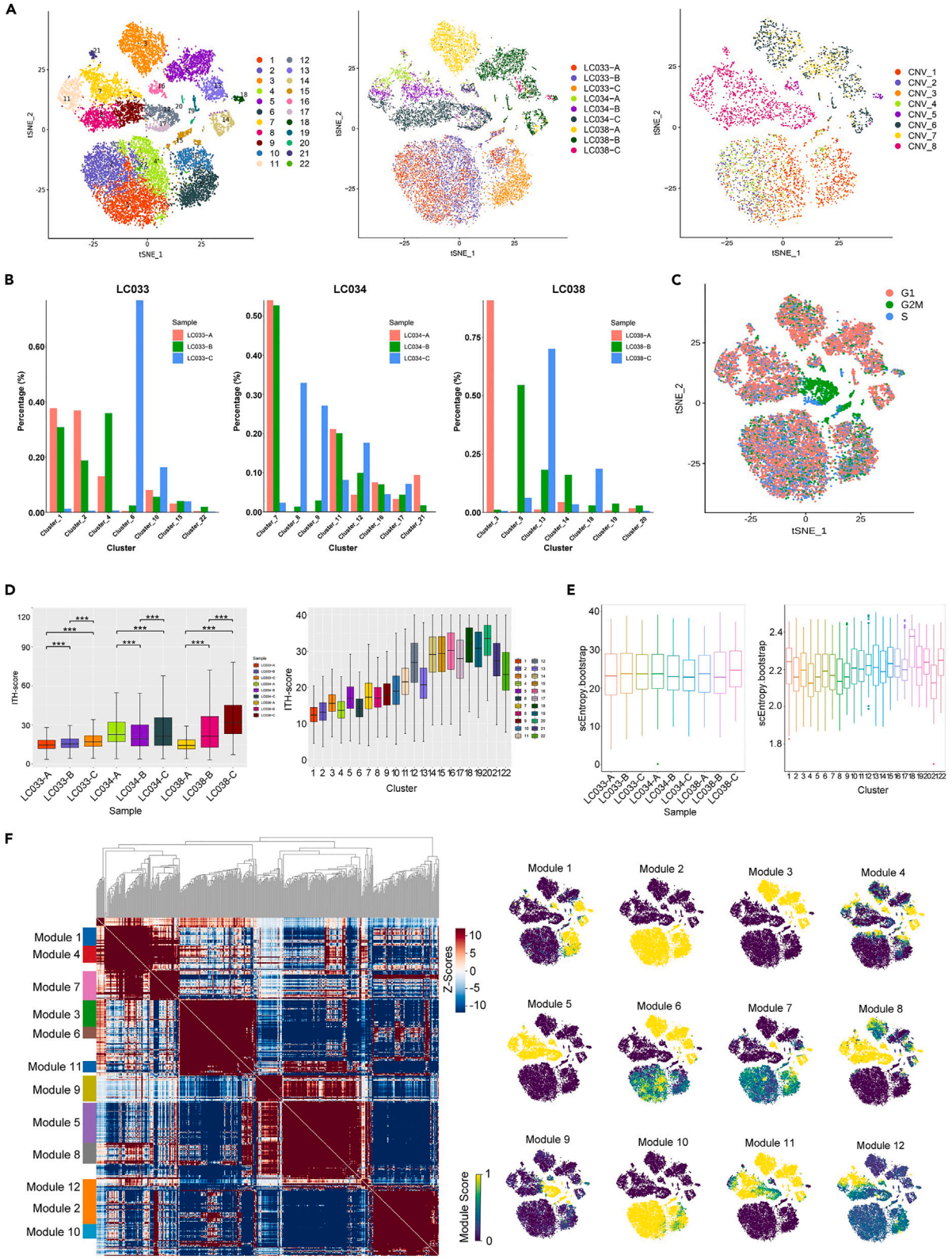
A
tSNE_1
tSNE_2
LC033-A
LC033-B
LC033-C
LC034-A
LC034-B
LC034-C
LC038-A
LC038-B
LC038-C
CNV_1
CNV_2
CNV_3
CNV_4
CNV_5
CNV_6
CNV_7
CNV_8
B
LC033
LC034
LC038
Sample
Percentage (%)
Cluster
C
G1
G2M
S
D
ITH-score
Sample
Cluster
E
scEntropy bootstrap
F
Module 1
Module 2
Module 3
Module 4
Module 5
Module 6
Module 7
Module 8
Module 9
Module 10
Module 11
Module 12
Z-Scores
Module Score

Figure 2. Cancer cell clusters and Tumor heterogeneity analysis in HCC

(A) t-SNE plot of cancer cell clusters, sample origin, and CNV clustering.

(B) Histogram showing clusters of cancer cells distributed in different spatial locations.

(C) t-SNE plot showing cell cycle by color in cancer cells.

(D) Boxplot showing ITH-score of cancer cells from 9 samples (LC033-A/B/C, LC034-A/B/C, and LC038-A/B/C) and 22 cancer cells clusters (cluster 1–22).

(E) scEntropy bootstrap of cancer cells from 9 samples (LC033-A/B/C, LC034-A/B/C, and LC038-A/B/C) and 22 cancer cells clusters (cluster 1–22).

(F) NMF analysis of cancer cells. Left, heatmap showing correlation of all modules derived from NMF analysis of 22 cancer cell clusters; 12 highly correlated modules are highlighted. Right, t-SNE plot of highlighted 12 modules. Data are represented as mean ± SEM; ***p<0.001.

and these cells were in a hyperproliferative state. This feature is consistent with the characteristics of LCSCs.[20]

We performed intratumoral heterogeneity score (ITH-score)[21] to calculate the stemness of cancer cells (Figures S7A, and 2D). LC033 and LC038 had the strongest tumor heterogeneity at point C, gradually increasing from tumor center to margin. The heterogeneity of Cluster 11–22 is higher than Cluster 1–10 (Figure 2D). In addition, scEntropy[22] was used to analyze the entropy value of cancer cells (Figures S7B and 2E). Entropy is negatively correlated with cell differentiation status; high entropy is correlated with higher potential (stemness). The results of scEntropy were consistent with ITH-score. Clusters 1, 10, 12, 13, 15, 16, 17, 18, 19, 20, and 22 showed higher stemness (Figure 2E).

Then, we used the consensus non-negative matrix factorization (cNMF)[23] to perform functional clustering of cancer cells, which are divided into 12 modules (Figure 2F). Among them, Module 1, 4 and 7 were related to immunity (antigen processing and presentation of peptide antigen via MHC class II, microglial cell activation, Antigen processing and presentation, Th17 cell differentiation, Th1 and Th2 cell differentiation, Phagosome, macrophage activation, myeloid leukocyte migration, phagocytosis) (Figure S7C). Cancer cells related to immunity include Cluster 6, 10, 13, 14, 16, 18 (Figures 2A and 2F). More importantly, Module 9 is related to Cell cycle, p53 signaling pathway, Cellular senescence, Platinum drug resistance, etc. (Figure S7D). Cancer cells related to module 9 are Cluster 12, 15, 17, 20 (Figures 2A and 2F). Combined with the above results, these cells were found to be liver cancer stem-like cells (LCSCs).[24–26] The distribution of Module 9 in the spatial position showed that it gradually increased from A to B and then to C (Figure S7E). Collectively, we explored the cancer cells heterogeneity of HCC by multiple methods and found LCSCs in the cancer cells at the tumor margin.

TOP2A and *CENPF* maintain the stemness of LCSCs

Then, monocle 2[27] was used to perform trajectory analysis on cancer cells (Figure 3A). The pseudotime trajectory axis derived from cancer cells of LC033 indicated that Cluster 6 and 10 transdifferentiate into Cluster 2 and 4 then into Cluster 15 (Figures 3A, and S8A); LC034 took Cluster 16 as a starting point for development into Cluster 12 and 17 (Figures 3A, and S8B); Cluster 13, 14 and 18 together serve as the starting point for the evolution of LC038 cancer cells, and trajectory transdifferentiate into Cluster 20 (Figures 3A and S8C). What's more, pseudotemporal expression dynamics of specific representative genes also marked the progression of cancer cells (Figure S9). According to CNV analysis of cancer cells (Figure S10), we drew the CNV phylogenetic tree and found that Clusters 10, 16, 18 were located at the beginning of the tree (Figure 3B). As the accumulation of subclonal changes, Clusters 1, 12, 15, 17, 20 were at the end of the tree branches (Figure 3B), which is consistent with the results of trajectory analysis. In general, through the developmental analysis of cancer cells, we found that early tumor-initiating cells (TICs, Cluster 6, 10, 13, 14, 16, 18) eventually evolved into highly malignant LCSCs (Cluster 12, 15, 17, 20). LCSCs generated during tumor progression further promote the tumor heterogeneity of HCC.[28] GSEA scores showed that the above subclusters had higher stemness scores than other subgroups (Figure S11).

To further explore LCSCs (cluster 12, 15, 17, 20), we analyzed the specifically expressed genes in HCC subclusters (Figures S12A–S12C). GSVA analysis found that Clusters 10, 14, 16, 18 are enriched in allograft rejection, which is related to immune response; Cluster 12, 15, 17, 20 are enriched in cell cycle and DNA replication (Figure S12D). Genes expressed specifically in LCSCs (132 genes) were selected for research (Figure 3C). Functional enrichment analysis confirms these genes were enriched in apoptosis, p53 signaling pathway, Drug metabolism, Pyrimidine metabolism, Cell cycle (Figure S13A). We can see that the above functions are related by drawing a function network diagram and their core functions were cell cycle and drug metabolism (Figure S13B). The genes with the most significant differences were *CENPF*, *TOP2A*, *NUSAP1*, *MKI67*, *CENPU* (Figure 3D). Among them, TOP2A and CENPF specifically expressed in LCSCs

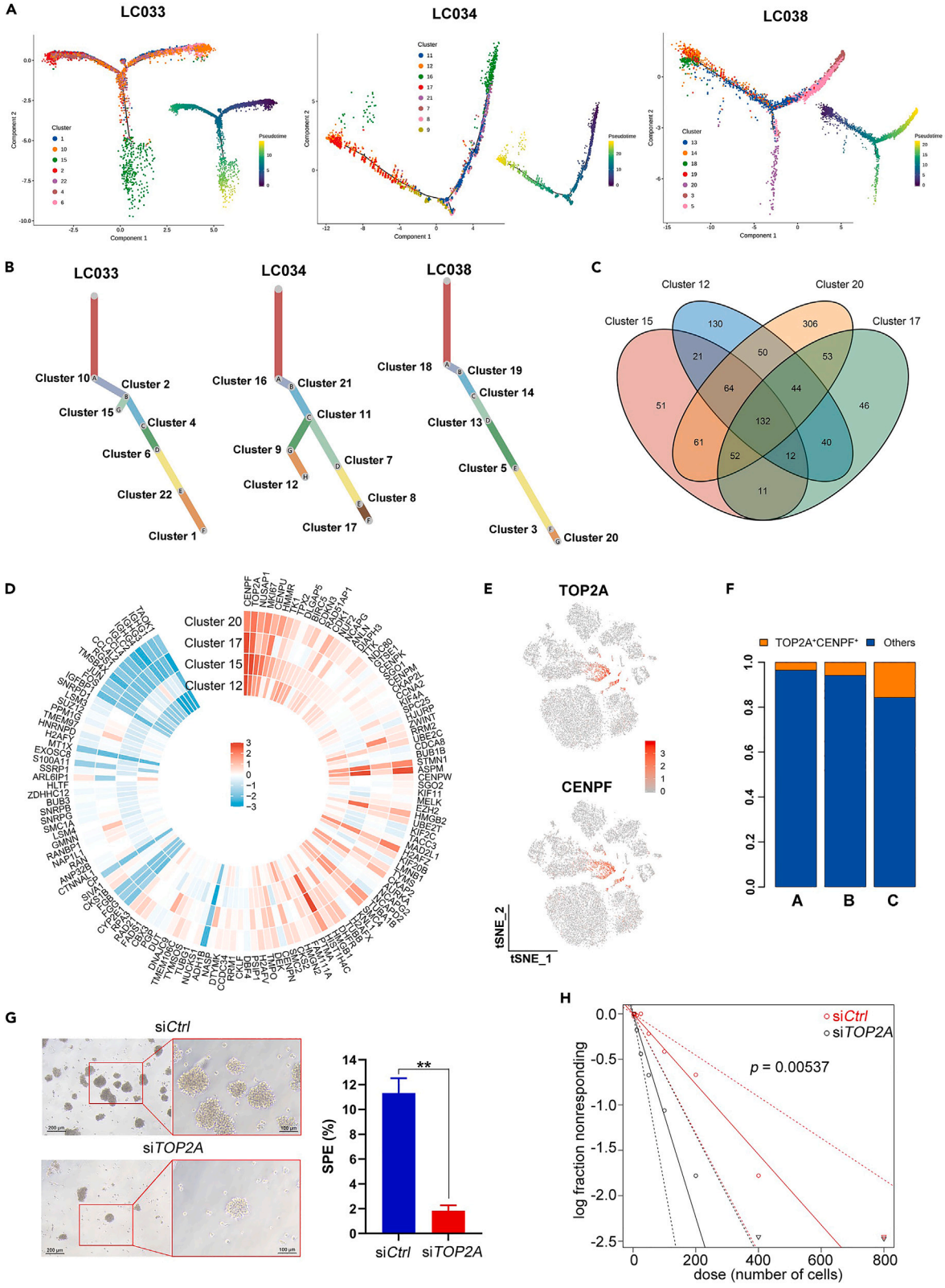
A
LC033
LC034
LC038
Component 1
Component 2
Cluster
Pseudotime
B
LC033
LC034
LC038
Cluster 10
Cluster 2
Cluster 15
Cluster 4
Cluster 6
Cluster 22
Cluster 1
Cluster 16
Cluster 21
Cluster 11
Cluster 9
Cluster 7
Cluster 12
Cluster 8
Cluster 17
Cluster 18
Cluster 19
Cluster 14
Cluster 13
Cluster 5
Cluster 3
Cluster 20
C
Cluster 12
Cluster 20
Cluster 15
Cluster 17
130
306
21
50
53
64
44
51
46
132
61
40
52
12
11
D
Cluster 20
Cluster 17
Cluster 15
Cluster 12
E
TOP2A
CENPF
tSNE_1
tSNE_2
F
TOP2A⁺CENPF⁺
Others
A
B
C
G
siCtrl
siTOP2A
SPE (%)
**
H
siCtrl
siTOP2A
p = 0.00537
log fraction nonresponding
dose (number of cells)

Figure 3. Analysis of cancer cells transition states and the main factors to maintain the stemness of LCSCs

(A) Potential developmental trajectory of malignant cells of LC033, LC034 and LC038 inferred by analysis with Monocle 2. Each point corresponded to one cell. Cells were colored based on their cluster.

(B) Clonality trees of 3 patients separated by gene expression profile class. The branches are scaled according to the percentage of cells in the calculated subclone containing the corresponding CNV. The length of the branches of the evolutionary tree represents the number of cells of the subcloned.

(C) Venn diagram showing 132 genes co-expressed by Cluster 12, 15, 17, 20.

(D) Circular heatmap showing 132 genes expressed by Cluster12, 15, 17, 20.

(E) t-SNE plot, gray to red color coding for the expression of the marker genes (*TOP2A* and *CENPF*) for the indicated cell subtype.

(F) Histogram indicating the proportion of *TOP2A*$^{+}$*CENPF*$^{+}$ cancer cells in A/B/C.

(G) Tumorspheres assays revealed the stemness of HCC cells treated with si-*TOP2A* or si-*CENPF*. Representative image of sphere formation assays under light microscope (200× and 400×).

(H) The limiting dilution assays revealed the neurosphere-forming capacity of different LCSC groups after TOP2A knockdown treatment. Data are represented as mean ± SEM; **p<0.01.

have expression differences, clinical differentiation, prognostic value and diagnostic value (Figures 3E and S14A–S14I).

Consistently, the ratio of *TOP2A*$^{+}$*CENPF*$^{+}$ cells from A, B and C was detected and we found that it gradually increased from the center to the margin of the tumor (Figure 3F). We selected the same samples for immunohistochemistry (IHC) and found that *TOP2A* and *CENPF* expression did increase gradually from the center to the margin (Figure S15A and S15B). And TOP2A/CENPF showed association with HCC stem cell genes in HCC cohort[29,30] (Figure S16). Then, we compared the expression of *TOP2A* and *CENPF* in different HCC cell lines (Figures S17A and S17B). The CCK-8 analysis proved that compared with the control group, both *TOP2A* and *CENPF* knockdown inhibited the proliferative capacity of HCC cells (Figure S17C). The test of stemness showed that knockdown of *TOP2A* and *CENPF* reduced the spheroidization rate of HCC cell lines (Figures 3G, and S17D). Further limiting dilution assay showed that the sphere formation capacity in *TOP2A* knockdown cancer cells was obviously diminished (Figure 3H). Together, these results suggest that *TOP2A* can promote the malignant phenotype of LCSCs *in vitro*.

In addition, we also explored the specific genes of immune-related TICs (Module 1, 4 and 7 in cNMF). The co-expressed genes of Cluster 6, 10, 13, 14, 16, 18 are *CCL5*, *CD52*, *TMSB10*, *TMSB4X*, *S100A4*, *HCST* (Figure S18A). These genes are all related to immunity and exist specifically in immune-related cancer cells (Figures S18B and S18C). Consistent with the distribution of cancer cells (Figure 2B), *CCL5* and *CD52* were highly expressed at the tumor margin (increasing from A to C), whereas no expression was detected in the non-tumor areas (Figures S18D and S18E).

In summary, *TOP2A* are not only special genes that maintain/promote the stemness of HCC cells, but also serve as new markers for LCSCs. Most previous studies believe that there are more CSCs in the cancer center.[31] However, in our observations, there are more cancer cells with high stemness at the margin of HCC.

Spatial distribution of immune cells in HCC

The appearance of LCSCs at the margin of solid tumors may be because of the abundant enrichment of immune cells.[32] Subsequently, we analyzed T cells (18013 cells, Figures S19–S21), B cells (5,288 cells, Figures S22–S24) and myeloid cells (22,455 cells, Figures S25 and S26) separately at the single-cell level and mapped the landscape of immune cells in the TIME.

Proliferative_T cells and Treg cells, which showed exhausted state of late development, were the majority T cells in the tumor (Figures S19E and S19F). Those cells were called exhausted T cells (exT).[33] However, CD8 effector T cells with immune efficacy were rejected from the tumor (Figures S19E and S19G). Intratumoral B cells are mainly plasma cells, enriched in oxidative phosphorylation, which is associated with the glycolytic process[34] required for abnormal B cell differentiation (Figures S22C–S22H). In addition, we observed interpatient specificity of plasma cells (Figures S22A–S22C). Collectively, these results revealed spatial heterogeneity of T cells and B cells.

Myeloid cells are the most abundant immune cells of the captured cells, which were classified as 11 Clusters (Figures 4A and S25). Subsequently, we performed a secondary classification of macrophages and KCs and found that *CD168*$^{+}$ macrophages are mainly in tumor (Figure 4B). Previous studies have suggested that classically activated macrophages (M1) and alternatively activated macrophages (M2) play different roles

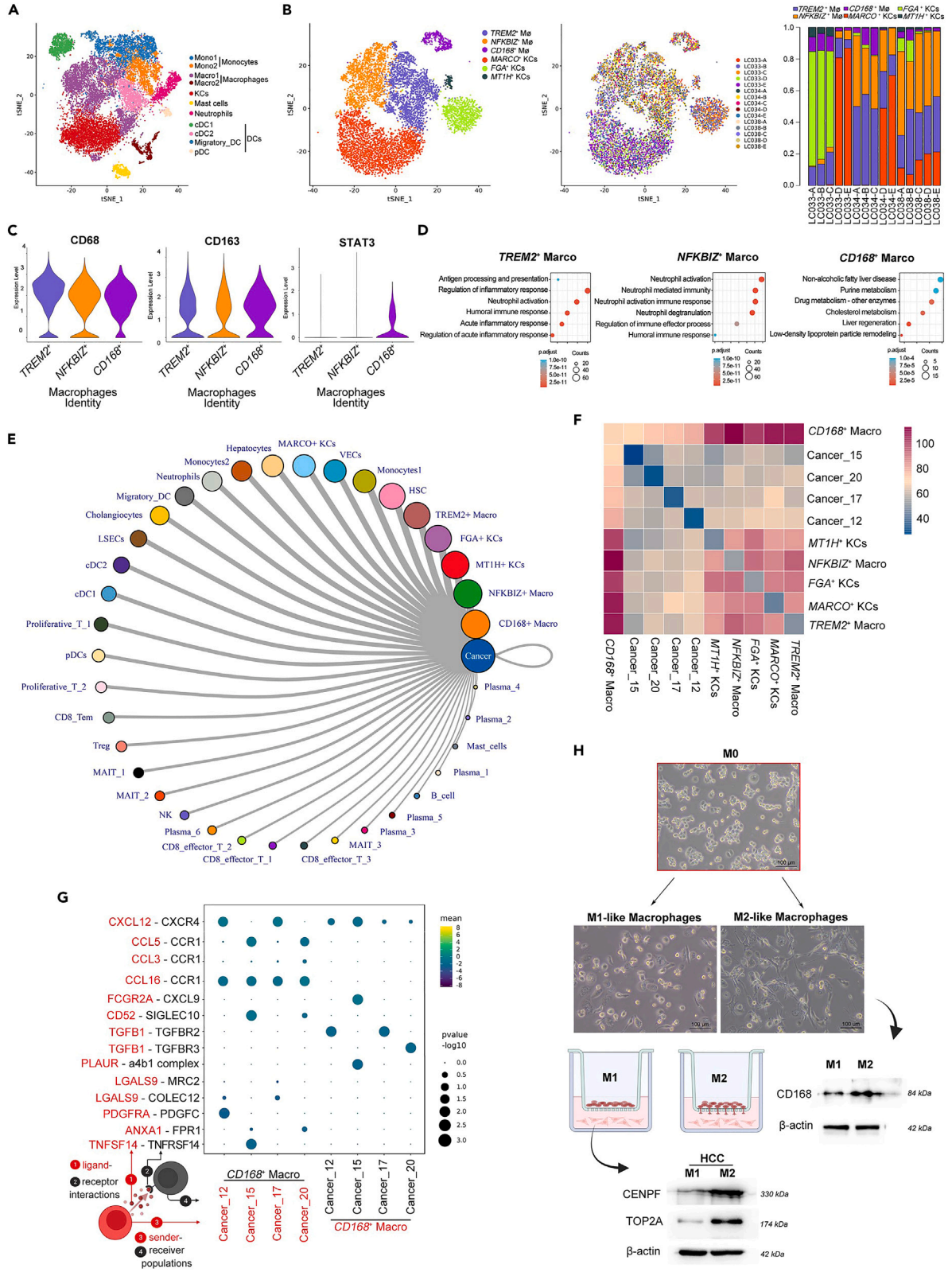
A
Mono1
Mono2
Monocytes
Macro1
Macro2
Macrophages
KCs
Mast cells
Neutrophils
cDC1
cDC2
Migratory_DC
DCs
pDC
tSNE_1
tSNE_2
B
TREM2+ Mø
NFKBIZ+ Mø
CD168+ Mø
MARCO+ KCs
FGA+ KCs
MT1H+ KCs
C
CD68
CD163
STAT3
Expression Level
TREM2+
NFKBIZ+
CD168+
Macrophages Identity
D
TREM2+ Marco
Antigen processing and presentation
Regulation of inflammatory response
Neutrophil activation
Humoral immune response
Acute inflammatory response
Regulation of acute inflammatory response
NFKBIZ+ Marco
Neutrophil activation
Neutrophil mediated immunity
Neutrophil activation immune response
Neutrophil degranulation
Regulation of immune effector process
Humoral immune response
CD168+ Marco
Non-alcoholic fatty liver disease
Purine metabolism
Drug metabolism - other enzymes
Cholesterol metabolism
Liver regeneration
Low-density lipoprotein particle remodeling
p.adjust
Counts
E
Hepatocytes
MARCO+ KCs
VECs
Monocytes2
Monocytes1
Neutrophils
HSC
Migratory_DC
TREM2+ Macro
Cholangiocytes
FGA+ KCs
LSECs
MT1H+ KCs
cDC2
NFKBIZ+ Macro
cDC1
CD168+ Macro
Proliferative_T_1
Cancer
pDCs
Plasma_4
Proliferative_T_2
Plasma_2
CD8_Tem
Mast_cells
Treg
Plasma_1
MAIT_1
B_cell
MAIT_2
Plasma_5
NK
Plasma_3
Plasma_6
MAIT_3
CD8_effector_T_2
CD8_effector_T_1
CD8_effector_T_3
F
CD168+ Macro
Cancer_15
Cancer_20
Cancer_17
Cancer_12
MT1H+ KCs
NFKBIZ+ Macro
FGA+ KCs
MARCO+ KCs
TREM2+ Macro
G
CXCL12 - CXCR4
CCL5 - CCR1
CCL3 - CCR1
CCL16 - CCR1
FCGR2A - CXCL9
CD52 - SIGLEC10
TGFB1 - TGFBR2
TGFB1 - TGFBR3
PLAUR - a4b1 complex
LGALS9 - MRC2
LGALS9 - COLEC12
PDGFRA - PDGFC
ANXA1 - FPR1
TNFSF14 - TNFRSF14
mean
pvalue -log10
1 ligand-
2 receptor interactions
3 sender-
4 receiver populations
CD168+ Macro
Cancer_12
Cancer_15
Cancer_17
Cancer_20
H
M0
M1-like Macrophages
M2-like Macrophages
M1
M2
CD168
β-actin
84 kDa
42 kDa
HCC
CENPF
TOP2A
330 kDa
174 kDa

Figure 4. Cell interaction network and multiple regulatory responses in the TME of HCC

(A) Myeloid cell clusters in HCC and ANT. t-SNE plot showing 11 clusters of 22,455 myeloid cells (indicated by colors).

(B) Macrophage clusters in HCC and ANT. Left, t-SNE plot showing 6 subclusters of macrophages/KCs cells (indicated by colors). Middle, t-SNE plot showing macrophages/KCs cell origins by color. Each color indicates one sample. Right, Histogram indicating the proportion of different cell types in the macrophages/KCs cells.

(C) Violin plot representing genes (*CD68*, *CD163*, *STAT3*) expression of 3 macrophages subclusters (*TREM2*$^+$ Macrophages, *NFKBIZ*$^+$ Macrophages, *CD168*$^+$ Macrophages).

(D) Bubble chart showing functional enrichment analysis of 3 macrophages subclusters (*TREM2*$^+$ Macrophages, *NFKBIZ*$^+$ Macrophages, *CD168*$^+$ Macrophages).

(E) The ranked differential tumor-immune cell crosstalk showing *CD168*$^+$ M2-like macrophages ranked the first among all ligand-receptor pairs.

(F) Heatmap showing number of potential ligand-receptor pairs between LCSCs groups and macrophages/KCs predicted by CellphoneDB.

(G) Bubble plots showing ligand-receptor pairs of cytokines between LCSCs groups and *CD168*$^+$ M2-like macrophages.

(H) Co-culture experiments showing that *CD168*$^+$ M2 macrophages promote the expression of *TOP2A* and *CENPF* in HCC cells.

in the TIME.[35] Through detecting the expression of *CD68*, *CD163* and *STAT3*,[36,37] we inferred that *CD168*$^+$ macrophages may be M2-like macrophages (Figure 4C). Functional analysis revealed that macrophages expressing *TREM2* and *NFKBIZ* showed higher expression levels of genes associated with antigen processing and presentation, and neutrophil activation, respectively. On the other hand, *CD168*$^+$ macrophages showed higher expression levels of genes associated with drug metabolism and cholesterol metabolism[38] (Figure 4D). Collectively, these results demonstrated spatial heterogeneity of immune cells and identified the *CD168*$^+$ macrophages as the M2-like macrophages in tumor.

CD168$^+$ M2-like macrophages increase tumor stemness by interacting with cancer cells

In order to explore specific mechanism, we used CellPhoneDB[39] to identify the interaction between cancer cells and other cells. First, we found that it was myeloid cells, not T cells or others, interacted most with cancer cells (Figures S27A–S27D). After further dividing the cell types, the interaction between *CD168*$^+$ macrophages and cancer cells was the strongest (Figure 4E). Interaction analysis of macrophages and LCSCs showed that *CD168*$^+$ macrophages had the strongest interaction with Cluster 12, 15, 17, 20 (Figure 4F). In ligand-receptor analysis, we observed that *CD168*$^+$ macrophages acted on LCSCs through CXCL12-CXCR4 and TGFB1-TGFBR2/3 (Figure 4G). Combining the above research, we can make a conjecture that M2-like macrophages promote the stemness of cancer cells through CXCL12 and TGF-β. In turn, we found LCSCs acted on *CD168*$^+$ macrophages through CCL16-CCR1 (Figure 4G). CCL16 secreted by cancer cells also contributes to tumor angiogenesis,[40] and helps metastasize. To validate this observation, we conducted a co-culture and found that the expression of *TOP2A* and *CENPF* in cancer cells with M2-like macrophages increased compared with the M1 group (Figure 4H).

Spatial feature analysis[41] showed that an increase in *TOP2A*$^+$ HCC cells at the margin of HCC, accompanied by the presence of *CD168*$^+$ macrophages (Figures 5A, 5B, and S28). To further verify the role of macrophages in promoting HCC stemness, we isolated macrophages from HCC tumor (T) and adjacent normal tissues (N) (Figure 5C). CXCL12 levels were significantly elevated in M2 macrophage culture supernatants at 48 and 72 h (Figure 5D). TGF-β1 showed the same result. TOP2A expression was higher in HCC cells co-cultured with tumor tissue-derived macrophages than in normal tissues (Figure 5E). Co-culture with macrophages from tumor tissue will significantly increase the proliferation and sphere formation capacity of LCSCs (Figures 5F and 5G). Together, these results suggest intratumoral macrophages may promote the stemness of HCC cells through CXCL12 and TGF-β1, leading to the formation of LCSCs.

Of interest, we observed that TICs (Cancer 6, 10, 13, 14, 16, 18) act on *CD168*$^+$ macrophages via CCL3, CCL5, CCL16, and NAMPT[42] (Figure S27E), indicating their important roles in recruiting M2-like macrophages to the tumor margins. Collectively, *CD168*$^+$ M2-like macrophages, recruited by TICs, play a role in promoting tumor stemness through cell interaction with cancer cells in TIME.

TOP2A promotes HCC progression *in vitro* and *in vivo*

To determine the biological functions of *TOP2A* in HCC cells, we first constructed TOP2A knockdown and control in the HCC cell lines according to the expression of *TOP2A* (Figures 6A, and S17B). CCK-8 and colony formation experiments verified that the proliferative capacity of HCC cells was inhibited in *TOP2A* knockdown group (Figures 6B and 6C). Western blot showed that knockdown *TOP2A* reduced the expression of Ki-67 (Figure 6D). In addition, we found that HCC cells transfected with si-*TOP2A* had an obvious cell-cycle arrest at S phase (Figure 6E). Moreover, cyclin A1 was decreased in TOP2A knockdown cells

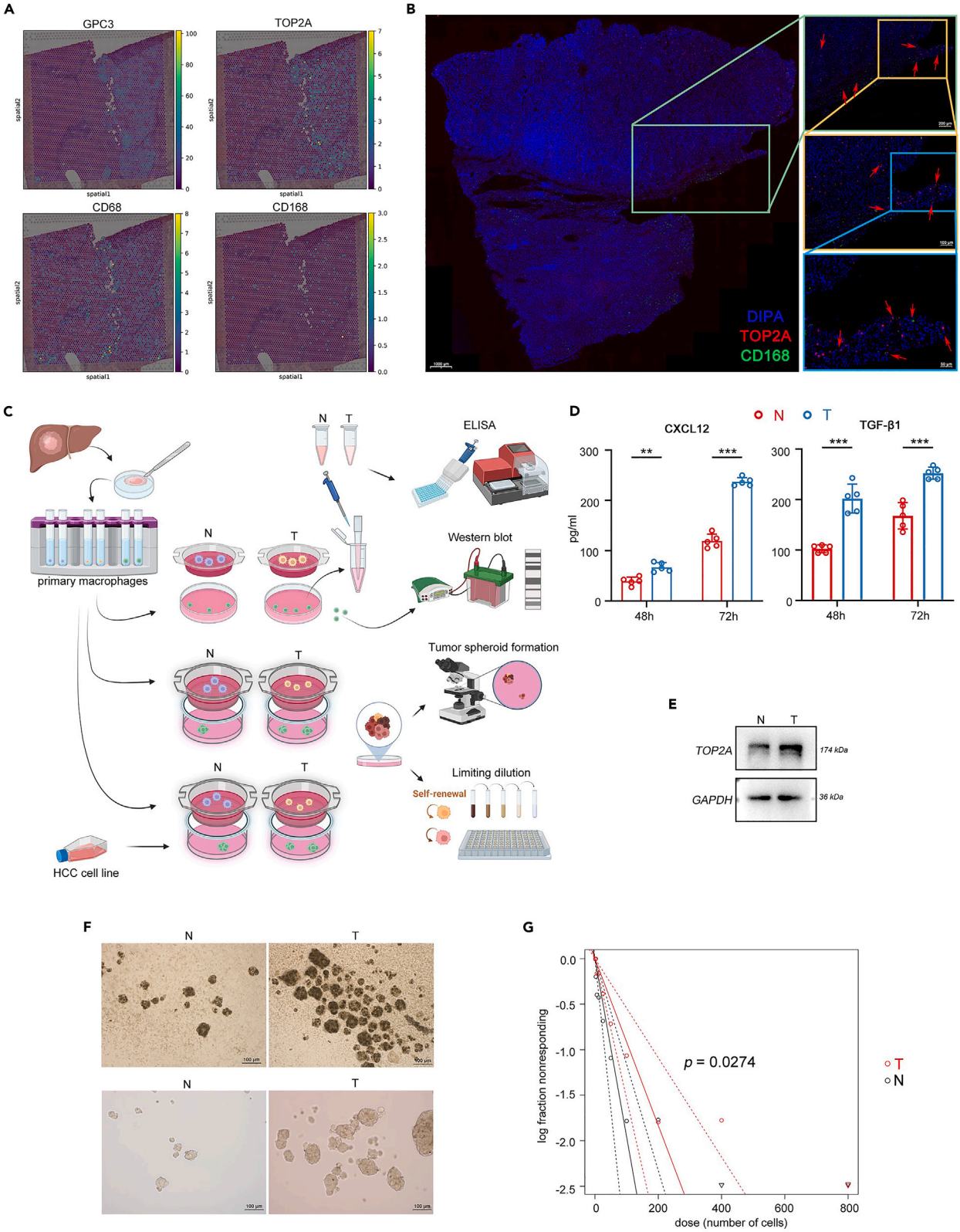
A
GPC3
TOP2A
CD68
CD168
spatial1
spatial2
B
DIPA
TOP2A
CD168
C
primary macrophages
HCC cell line
ELISA
Western blot
Tumor spheroid formation
Limiting dilution
Self-renewal
N
T
D
CXCL12
TGF-β1
pg/ml
48h
72h
E
TOP2A
GAPDH
174 kDa
36 kDa
F
G
p = 0.0274
log fraction nonresponding
dose (number of cells)

Figure 5. Tumor-derived macrophages promote HCC cell stemness

(A) Spatial transcriptome analysis revealed the presence of *TOP2A*$^+$ cells and *CD168*$^+$ macrophages at the tumor margin.

(B) Multicolor immunofluorescence showed the presence of *TOP2A*$^+$ cells in the tumor margin, accompanied by *CD168*$^+$ cells.

(C) Schematic diagram of tumor primary macrophage extraction and stemness experiment.

(D) Histogram shows the levels of CXCL12 and TGF-β1 in the co-cultured tumor cell supernatant detected by ELISA assay.

(E) Western blot showed that co-culture with tumor-derived macrophages promoted the expression of TOP2A.

(F) Tumorspheres assays revealed the stemness of HCC cells treated with T-macrophages or N-macrophages. Representative image of sphere formation assays under light microscope (200× and 400×).

(G) The limiting dilution assays revealed the neurosphere-forming capacity of different LCSC groups after co-culture with T-macrophages or N-macrophages. Data are represented as mean ± SEM; ***p<0.001, **p<0.01.

(Figure S29A). Furthermore, Flow cytometry analysis showed that the *TOP2A* knockdown increased the apoptosis rate of HCC cells (Figure S29B). Subsequently, cells stably transfected with sh-Ctrl or sh-*TOP2A* were inoculated subcutaneously into SCID mice and were monitored closely for tumor growth for 20 days. We found that tumors derived from sh-*TOP2A* cells were smaller than those derived from sh-*Ctrl* transfected cells (Figure S29C), in terms of both tumor volume and weight (Figure 6F). IHC showed that compared with the sh-Ctrl group, the expression of Ki67 in the sh-*TOP2A* group was distinctly reduced (Figure 6G). These findings indicated that TOP2A knockdown inhibits the progression of HCC.

To further investigate the effects of *TOP2A* on HCC, we selected SK-HEP-1 (TOP2A low expression) to transfect the empty vector plasmid (Ctrl group) and the TOP2A recombinant plasmid (TOP2A group) respectively (Figures S30A and S30B). Then, we found that *TOP2A* overexpression promoted HCC progression *in vitro* and *in vivo* (Figures S30C–S30L). Collectively, these results identified *TOP2A* as oncogene for HCC progression.

TOP2A affects HCC tumor progression through hippo signaling pathway

GSEA showed that *TOP2A* expression positively correlated with Hippo pathway and cell cycle (Figure 7A). Hippo is a signaling pathway closely related to tumor stemness discovered in recent years.[43] Therefore, we speculated that TOP2A exerted HCC stemness promoting effects through Hippo pathway.

Verteporfin (VP), an inhibitor of the Hippo pathway, has been reported to prevent the binding of YAP and TEAD4.[44] We found that VP inhibited the stemness and proliferation of HCC cell lines, and reversed the TOP2A-mediated promoting effects on HCC cells (Figures 7B–7D). VP partly reversed TOP2A-induced regulation effect on cell cycle (Figure 7E). In addition, VP increased the HCC cells apoptosis rate, which was decreased by *TOP2A* overexpression (Figure S31). Altogether, these results demonstrated that TOP2A promotes HCC development primarily by inactivating Hippo signaling pathway.

The binding of TOP2A to β-catenin promotes the entry of YAP1 into the nucleus

Subsequently, we found that knocking down *TOP2A* decreased YAP1 and p-YAP1 (Figures 8A and 8B). In contrast, *TOP2A* overexpression up-regulated the protein levels of *YAP1* and p-YAP1 (Figures S32A and 8C). It has been shown that, when the Hippo pathway is inactivated, YAP is not phosphorylated and translocates into the nucleus together with TAZ, forming a complex with TEAD4. This complex can activate the expression of target genes related to cell proliferation, thereby promoting cell proliferation.[45] Consistently, TOP2A and TEAD4 are mainly in the nucleus, p-YAP1 in the cytoplasm, and YAP1 and TAZ both in the cytoplasm and nucleus (Figures S32B and 8D). Protein-protein interaction results indicated that β-catenin played an important role in the effect of TOP2A on the Hippo signaling pathway (Figures 8E and S32C). Subsequently, knocking down *TOP2A* increased β-catenin and YAP1 in the cytoplasm (Figure 8F), indicated β-catenin may translocate out of the nucleus to interact with YAP1. No significant change was observed in TEAD4. Conversely, the *TOP2A* overexpression induced high expression of β-catenin and YAP1 in the nucleus (Figure 8G). Based on the above, we hypothesized that β-catenin directly binds to TOP2A in the nucleus and YAP1 in the cytoplasm separately. The co-immunoprecipitation (co-IP) was used to confirm this. We performed an IP using a β-catenin construct in MHCC97L and Hep3B2.1-7, and successfully pulled down TOP2A and YAP1 (Figure 8H).

In addition, previous studies have suggested that TOP2A may be a downstream product of YAP1/TEAD4 transcriptional regulation.[46] We knocked down *TEAD4* and observed a significant reduction of TOP2A, whereas YAP1 and TAZ level were not changed (Figure S32D).

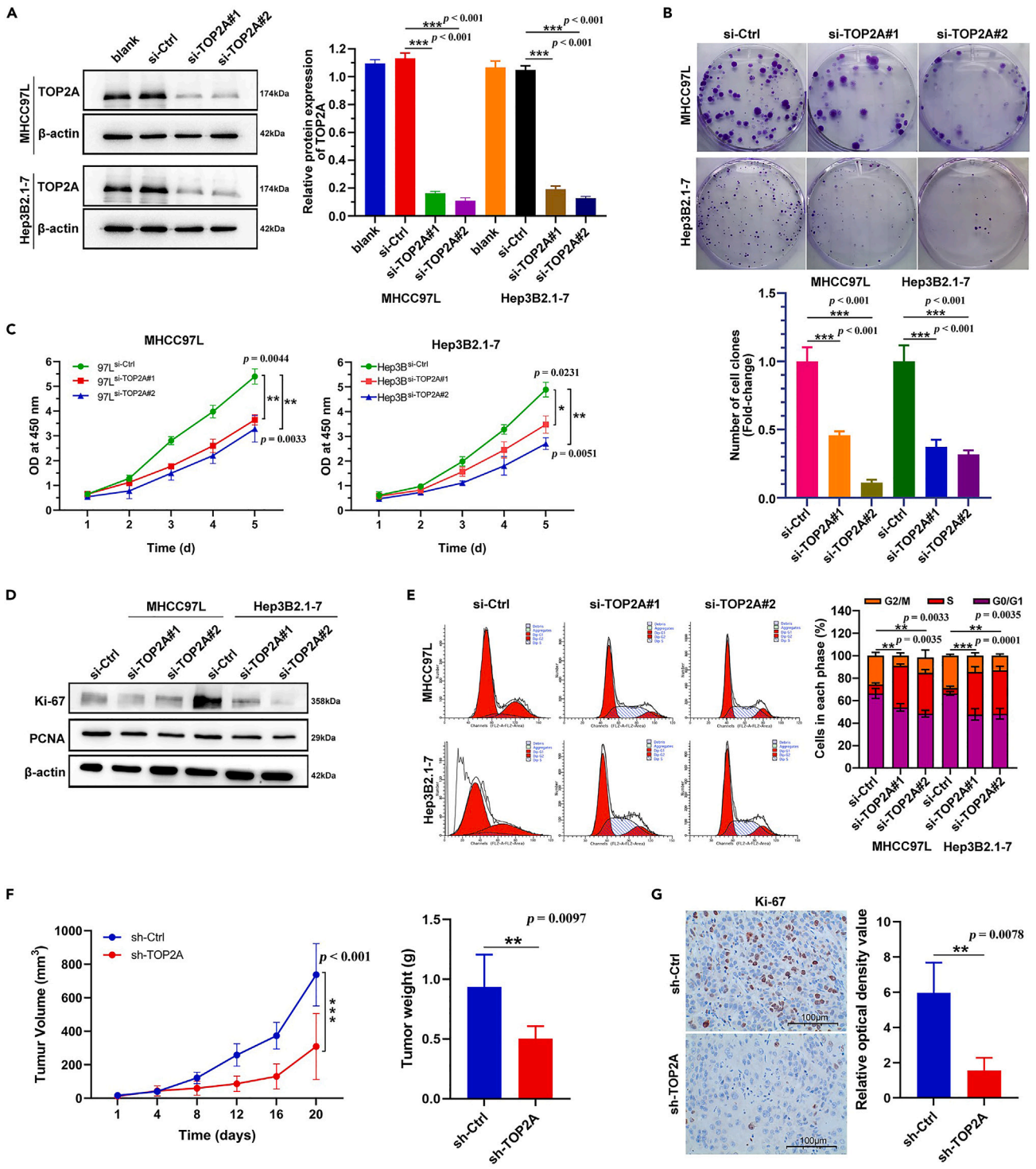

Figure 6. *TOP2A* knockdown inhibited the proliferation of HCC cell lines

(A) Western blot of *TOP2A* expression after transfection with MHCC97L and Hep3B2.1-7 (si*Ctrl*, si*TOP2A*#1 or si*TOP2A*#2).

(B) Downregulation of *TOP2A* reduced the mean colony number in the colony formation assay.

(C) CCK-8 assays revealed that downregulation of *TOP2A* decreased the growth rate of indicated cells.

(D) Western blot showed the expression of Ki67 and PCNA in MHCC97L and Hep3B2.1-7 cells after the knockdown of TOP2A.

(E) Flow cytometry to detect the cell cycle of HCC cells (MHCC97L and Hep3B2.1-7) transfected with si-Ctrl or si-TOP2A.

(F) Tumor growth and weight of tumors in xenograft mice injected with shTOP2A or control cells at the indicated times.

(G) The expression of Ki67 in tumors was determined by immunohistochemistry. Data are represented as mean ± SEM; ***p< 0.001, **p< 0.01, *p< 0.05.

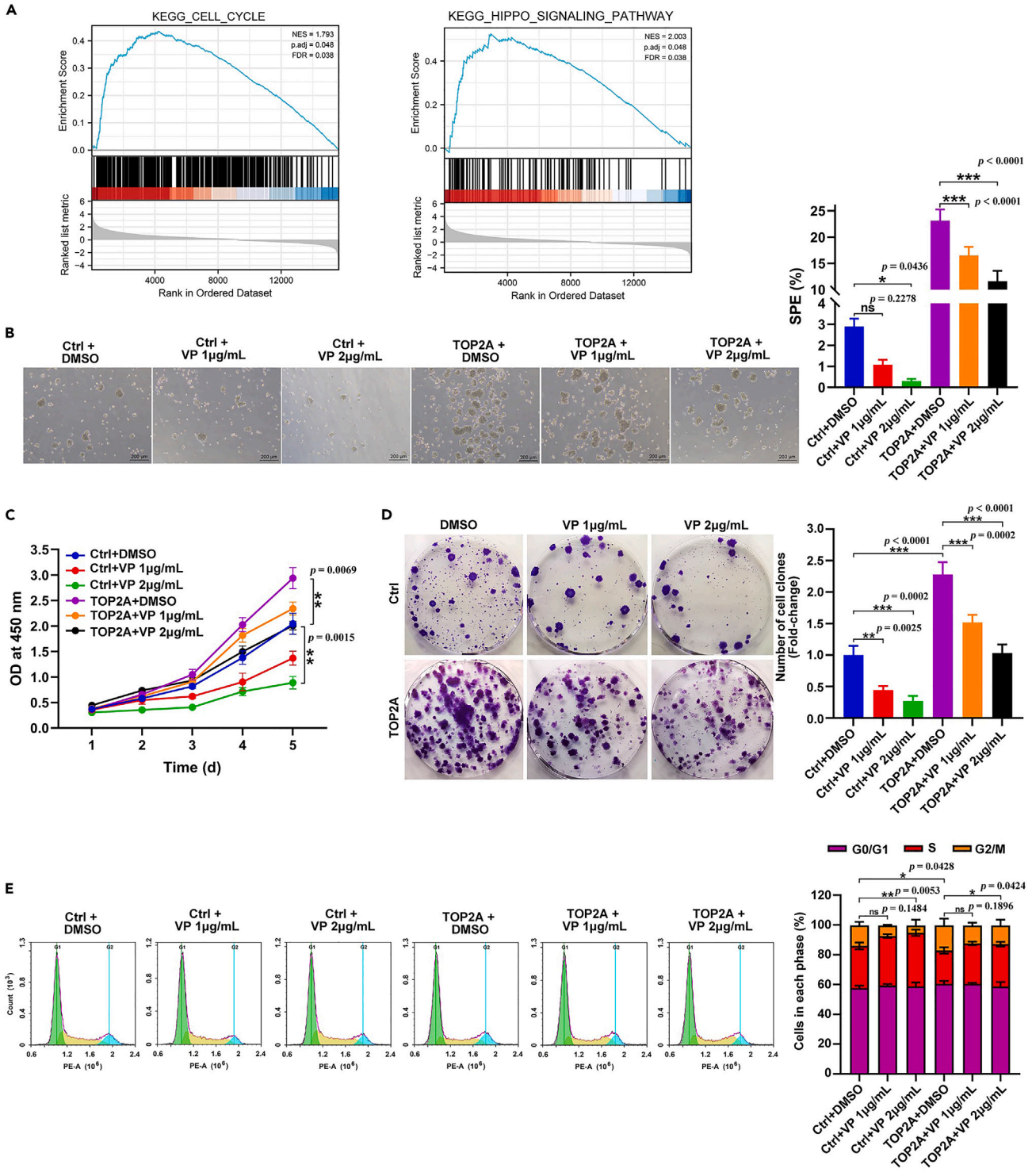

Figure 7. TOP2A affects HCC tumor progression through hippo signaling pathway

(A) Enrichment plots of cell cycle and hippo signing pathway from GSEA.

(B) Tumorspheres formation assays revealed the stemness of HCC cells treated with Ctrl+DMSO, Ctrl+VP 1ug/mL, Ctrl+VP 2ug/mL, TOP2A + DMSO, TOP2A + VP 1ug/mL, and TOP2A + VP 2ug/mL. Representative image of sphere formation assays under light microscope (200×).

(C) CCK-8 assays revealed the growth rate of HCC cells treated with Ctrl+DMSO, Ctrl+VP 1ug/mL, Ctrl+VP 2ug/mL, TOP2A + DMSO, TOP2A + VP 1ug/mL, and TOP2A + VP 2ug/mL.

Figure 7. *Continued*

(D) Colony formation assay revealed the growth ability of HCC cells treated with Ctrl+DMSO, Ctrl+VP 1ug/mL, Ctrl+VP 2ug/mL, TOP2A + DMSO, TOP2A + VP 1ug/mL, and TOP2A + VP 2ug/mL.

(E) Flow cytometry to detect the cell cycle of SK-1 cells treated with Ctrl+DMSO, Ctrl+VP 1ug/mL, Ctrl+VP 2ug/mL, TOP2A + DMSO, TOP2A + VP 1ug/mL, and TOP2A + VP 2ug/mL. Data are represented as mean ± SEM; ***p< 0.001, **p< 0.01, *p< 0.05.

Overall, these results indicated that TOP2A exerts a transcriptional regulatory function through competing to bind β-catenin and promote YAP1 translocation into the nucleus. As a downstream product of YAP1/TEAD4, TOP2A forms a loop with the Hippo signaling pathway.

DISCUSSION

In this study, we conducted an in-depth analysis of the spatial distribution patterns of cancer cells and immune cells. Our findings revealed that *TOP2A*$^+$*CENPF*$^+$ liver cancer stem cells (LCSCs) were primarily localized at the tumor periphery, whereas *CD168*$^+$ M2-like macrophages within the tumor microenvironment (TME) were identified as the key drivers of enhanced cancer stemness. Moreover, our data indicated that the overexpression of TOP2A in hepatocellular carcinoma (HCC) cells influenced the nuclear localization of YAP1 through β-catenin, ultimately resulting in a significant modulation of HCC stemness and progression.

The spatial heterogeneity is an important component of tumor heterogeneity.[47] What's more, the spatial heterogeneity of the tumor determines the progression of cancer and the response to treatment.[48] The main reason for the spatial heterogeneity of HCC is the heterogeneous distribution of cancer cells. Through trajectory analysis and cNMF, we found immune-related tumor-initiating cells (TICs, *CCL5*$^+$*CD52*$^+$ cancer cells) in the early stage, and liver tumor stem-like cells (LCSCs, *TOP2A*$^+$*CENPF*$^+$ cancer cells) in the late stage. The two types of cells play different roles.

Our research found that *CCL5*$^+$*CD52*$^+$ TICs secreting CCL3, CCL5, CCL16 recruited monocytes/macrophages from the peripheral circulation, and expressed *CD52* to avoid phagocytosis. Recent studies have shown that TICs promote tumor progression by establishing an immune-related niche signaling loop through IL-33-TGF-β in breast cancer.[49] Sun et al.[50] have discovered that *CCL5*$^+$HCC circulating tumor cells in peripheral blood promote their survival by interacting with Tregs. Therefore, the macrophages recruited by TICs may be one of the reasons for the immune imbalance of the TIME.

Many studies suggested that hypoxia and necrosis in the tumor center significantly promote tumor stemness.[51,52] However, our study found that LCSCs mainly appeared at the margin of solid tumors. We further explored the possible causes of LCSCs. We found that *CD168*$^+$ M2-like macrophages acted as tumor-associated macrophages (TAMs) to promote the production of LCSCs. Researchers have found that TAMs producing milk fat globule-epidermal growth factor-VIII (MFG-E8) and IL-6 synergistically activate STAT3 and sonic Hedgehog pathways in cancer cells, promoting their tumorigenicity.[53] In addition, TAMs interacted directly with CSCs via LSECtin-BTN3A3, and targeted blocking of this receptor-ligand interaction destroy the CSC pool.[54] These studies suggest that TAMs play a special role in CSC generation and cancer progression. The co-culture experiment of HCC cell line and macrophages also proved this conclusion.

Of interest, TICs and LCSCs have significant spatial distribution characteristics, both at the tumor margins. TICs at the margin of the tumor recruit peripheral monocytes/macrophages (mainly *CD168*$^+$ macrophages). *CD168*$^+$ M2-like macrophages promote the stemness of tumor-margin cells and generate LCSCs, leading to spatial heterogeneity of HCC. In addition, the pseudotime analysis of cancer cells gives us a unique differentiation trajectory. TICs recruit macrophages early in the process of their own evolution. The recruited macrophages help the cancer cells evolve into LCSCs, enhancing their proliferative capacity. In the process of long-term interaction between cancer cells and immune cells, they domesticate each other, resulting in the status of immunosuppression and evolution. To sum up, we describe this phenomenon on the spatial transcriptome map, which provides a unique perspective for the understanding of liver cancer. In addition, it is crucial to further investigate the distinct biomarkers of LCSCs closely associated with TOP2A, in order to enhance their clinical effectiveness.

In our research, T cells, B cells and myeloid cells exhibited spatial distribution characteristics. Previous studies have also found that *CD45*$^+$ cells in different sites (tumor, adjacent liver, hepatic lymph node, blood, and ascites) of liver cancer have specificity.[55] In addition, we have found that intratumoral T cell clusters

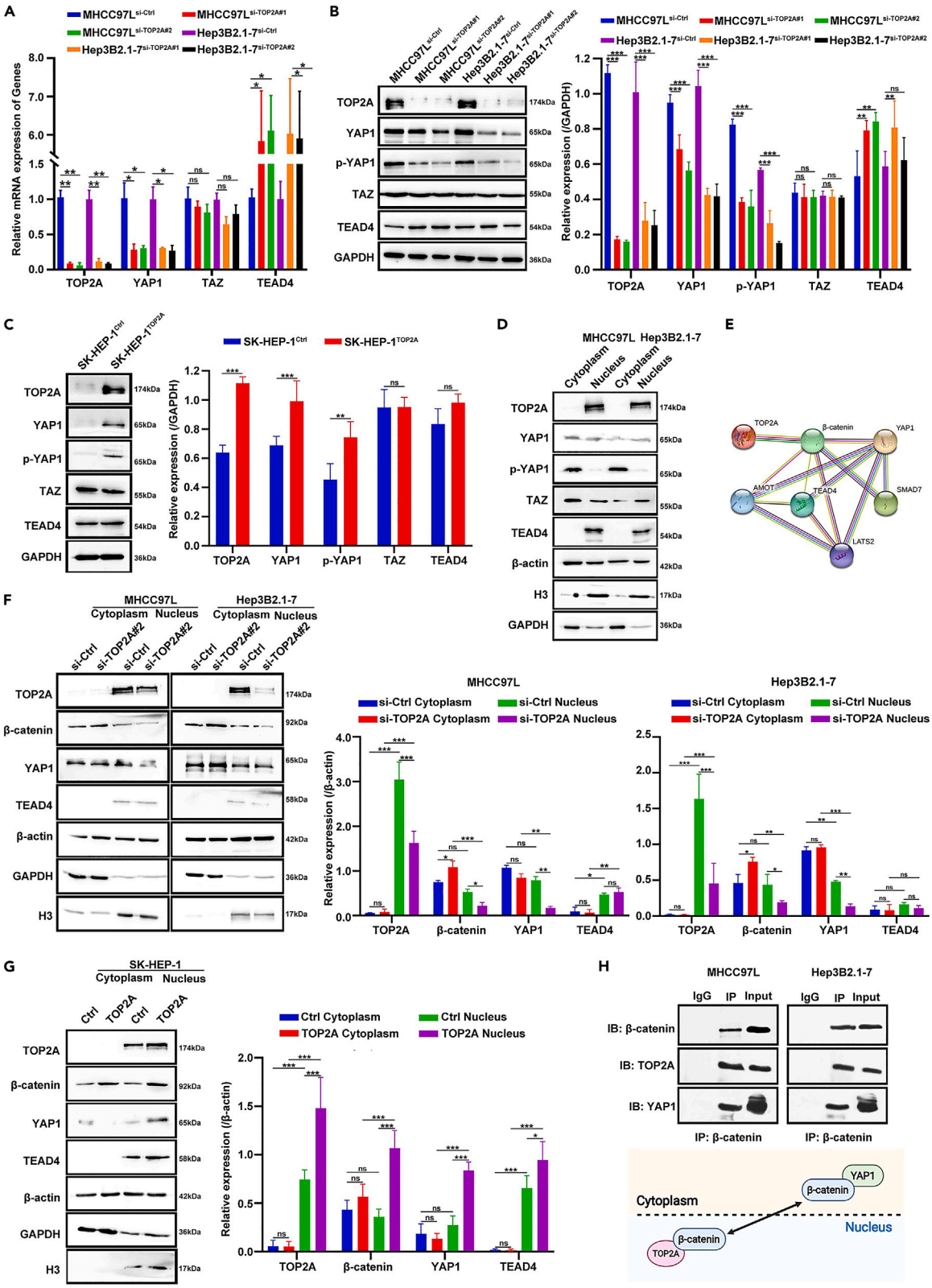
A
MHCC97L si-Ctrl
MHCC97L si-TOP2A#1
MHCC97L si-TOP2A#2
Hep3B2.1-7 si-Ctrl
Hep3B2.1-7 si-TOP2A#1
Hep3B2.1-7 si-TOP2A#2
Relative mRNA expression of Genes
TOP2A
YAP1
TAZ
TEAD4
B
TOP2A
YAP1
p-YAP1
TAZ
TEAD4
GAPDH
Relative expression (/GAPDH)
C
SK-HEP-1 Ctrl
SK-HEP-1 TOP2A
D
MHCC97L Hep3B2.1-7
Cytoplasm
Nucleus
β-actin
H3
E
β-catenin
AMOT
SMAD7
LATS2
F
MHCC97L
Hep3B2.1-7
si-Ctrl Cytoplasm
si-Ctrl Nucleus
si-TOP2A Cytoplasm
si-TOP2A Nucleus
Relative expression (/β-actin)
G
SK-HEP-1
Ctrl Cytoplasm
Ctrl Nucleus
TOP2A Cytoplasm
TOP2A Nucleus
H
IgG
IP
Input
IB: β-catenin
IB: TOP2A
IB: YAP1
IP: β-catenin
Cytoplasm
Nucleus

Figure 8. TOP2A directly affects YAP1 function through β-catenin

(A) qRT-PCR showed hippo pathway mRNA of indicated HCC cells (MHCC97L and Hep3B2.1-7) transfected with si-Ctrl or si-*TOP2A*.

(B) Western blot of hippo pathway protein of indicated HCC cells (MHCC97L and Hep3B2.1-7) transfected with si-Ctrl or si-*TOP2A*.

(C) Western blot of hippo pathway protein of indicated HCC cells (SK-HEP-1) transfected with TOP2A-vector (Ctrl group) or TOP2A (TOP2A group).

(D) Western blot shows the cytoplasmic and nuclear distribution of the proteins.

(E) STRING analysis of the correlation between TOP2A and the core protein of the hippo sign pathway.

(F) Western blot shows the cytoplasmic and nuclear separation of indicated HCC cells (MHCC97L and Hep3B2.1-7) transfected with si-Ctrl or si-TOP2A.

(G) Western blot shows the cytoplasmic and nuclear separation of indicated HCC cells (SK-HEP-1) transfected with TOP2A-vector (Ctrl group) or TOP2A (TOP2A group).

(H) co-IP shows that β-catenin directly binds to TOP2A and YAP1. Data are represented as mean ± SEM; ***p< 0.001, **p< 0.01, *p< 0.05.

displayed gene signatures associated with proliferative functions and T cell exhaustion, and the level of dysfunctional features is related to tumor therapy responsiveness, as described previously.[33]

Our results demonstrate that up-regulating *TOP2A* increased the transcription and translation levels of *YAP1*, which subsequently promotes downstream transcription of Hippo pathway. Previous studies have illustrated a crosstalk between the Wnt/β-catenin and Hippo signaling pathway, whereby YAP/TAZ inhibit Wnt/β-catenin signaling by preventing β-catenin's nuclear translocation without altering its stability.[56] We hypothesize that β-catenin acts as a mediator between TOP2A and the Hippo pathway.

Our findings reveal that TOP2A overexpression in HCC cells triggers the nuclear entry of β-catenin, leading to its dissociation from YAP1. Free YAP1 then forms a co-activating transcription factor with TEAD4, promoting the downstream transcription of the Hippo pathway. In contrast, TOP2A knockdown facilitates the binding of β-catenin to YAP1 in the cytoplasm, leading to YAP1 degradation after phosphorylation.[57] Overall, our findings suggest that TOP2A in HCC disrupts the regulation of the Hippo pathway through β-catenin. Mechanistically, TOP2A/β-catenin/YAP1 in HCC cancer cells promotes tumor stemness and progression. Furthermore, the downstream effects of YAP1 and β-catenin require additional validation through reporter gene assays or chip-Seq analyses.

Based on our research, early treatment targeting TICs prevents the accumulation of TAMs in the tumor environment. At the same time, reducing *CD168*$^+$ M2-like macrophage infiltration can inhibit the formation of LCSCs. The combined method is hopeful that by removing the soil where tumor cells grow, thus, LCSCs become more fragile and can be completely eradicated.

In summary, through multi-site scRNA-seq, we found that *CD168*$^+$ M2-like macrophages play an important role in the niche formed by LCSCs. In the process of cancer cell evolution, there is mutual domestication of cancer cells and immune cells. In addition, we identified TOP2A as a crucial oncogene in HCC progression. TOP2A acts on YAP1 through β-catenin to affect stemness and proliferation of HCC. The spatial heterogeneity of the HCC tumor microenvironment provides new insights for future treatments.

Limitations of the study

This study presents an innovative approach to investigate the spatial characteristics of HCC and LCSCs by scRNA-seq and *in vitro*/vivo experiments. However, some issues still require further investigation. Specifically, TOP2A was identified as a crucial regulator of stemness, but its limited clinical application because of its nuclear expression calls for the exploration of more specific markers closely associated with TOP2A. In addition, the downstream factors of TOP2A, β-catenin and YAP1, play a significant role, but their function as transcription factors warrants further exploration. Overall, our study and the above-mentioned findings have greatly enhanced our comprehension of HCC and LCSCs.

STAR★METHODS

Detailed methods are provided in the online version of this paper and include the following:

- KEY RESOURCES TABLE
- RESOURCE AVAILABILITY
  - Lead contact
  - Materials availability
  - Data and code availability
- EXPERIMENTAL MODEL AND SUBJECT DETAILS

SUPPLEMENTAL INFORMATION

Supplemental information can be found online at https://doi.org/10.1016/j.isci.2023.106862.

ACKNOWLEDGMENTS

This study was supported by the Shanxi Science and Technology Department (Grant No: 201903D421026, 201901D111404, 201901D211547), the Shanxi Health Commission (Grant No: 2019059), Shanxi Scholarship Council of China (Grant No: 2021-165), Shanxi Educational Department (Grant No: 2021Y359), and Shanxi '136' Leading Clinical Key Specialty (Grant No: 2019XY002). We are grateful to Changyu Chen (School of Foreign Languages, Xiangtan University) for the language modification suggestions of this article and BioRender.com for making the illustrations used in the study. We thank Kaiyue Lu and Peiquan Liang of Singleron for their help. We thank Helixlife for our experimental technical guidance. All experiment involving human tumor tissues and mice were approved by the institutional committee of Shanxi Bethune Hospital (No: YXLL-2019-83).

AUTHOR CONTRIBUTIONS

H.-C.Z. and C.-Z.C. designed and performed experiments, and wrote the paper; Y.-Z.T., H.-Q. S., Y.-J.L., and X.-X.W. performed experiments and analyzed data; J.-F.H. and H.-L.Z. provided human samples; J.-F.H. and Y.-Z.T. initiated and designed the study; H.-L.Z. initiated the study, organized, designed, and reviewed the paper. The authors read and approved the final manuscript.

DECLARATION OF INTERESTS

The authors have no conflicts of interest to declare based on the scope of this work.

INCLUSION AND DIVERSITY

We support inclusive, diverse, and equitable conduct of research.

Received: November 10, 2022
Revised: March 20, 2023
Accepted: May 8, 2023
Published: May 12, 2023

REFERENCES

1. Bray, F., Ferlay, J., Soerjomataram, I., Siegel, R.L., Torre, L.A., and Jemal, A. (2018). Global cancer statistics 2018: GLOBOCAN estimates of incidence and mortality worldwide for 36 cancers in 185 countries. CA A Cancer J. Clin. *68*, 394–424. https://doi.org/10.3322/caac.21492.

2. Siegel, R.L., Miller, K.D., Fuchs, H.E., and Jemal, A. (2021). Cancer statistics, 2021. CA A Cancer J. Clin. *71*, 7–33. https://doi.org/10.3322/caac.21654.

3. Zhang, Q., Lou, Y., Yang, J., Wang, J., Feng, J., Zhao, Y., Wang, L., Huang, X., Fu, Q., Ye, M., et al. (2019). Integrated multiomic analysis reveals comprehensive tumour heterogeneity and novel immunophenotypic classification in hepatocellular carcinomas. Gut *68*, 2019–2031. https://doi.org/10.1136/gutjnl-2019-318912.

4. Marusyk, A., and Polyak, K. (2010). Tumor heterogeneity: causes and consequences. Biochim. Biophys. Acta *1805*, 105–117. https://doi.org/10.1016/j.bbcan.2009.11.002.

5. Hyman, D.M., Taylor, B.S., and Baselga, J. (2017). Implementing genome-driven oncology. Cell *168*, 584–599. https://doi.org/10.1016/j.cell.2016.12.015.

6. Tirosh, I., Izar, B., Prakadan, S.M., Wadsworth, M.H., 2nd, Treacy, D., Trombetta, J.J., Rotem, A., Rodman, C., Lian, C., Murphy, G., et al. (2016). Dissecting the multicellular ecosystem of metastatic melanoma by single-cell RNA-seq. Science *352*, 189–196. https://doi.org/10.1126/science.aad0501.

7. Puram, S.V., Tirosh, I., Parikh, A.S., Patel, A.P., Yizhak, K., Gillespie, S., Rodman, C., Luo, C.L., Mroz, E.A., Emerick, K.S., et al. (2017). Single-cell transcriptomic analysis of primary and metastatic tumor ecosystems in head and neck cancer. Cell *171*, 1611–1624.e24. https://doi.org/10.1016/j.cell.2017.10.044.

8. Patel, A.P., Tirosh, I., Trombetta, J.J., Shalek, A.K., Gillespie, S.M., Wakimoto, H., Cahill, D.P., Nahed, B.V., Curry, W.T., Martuza, R.L., et al. (2014). Single-cell RNA-seq highlights intratumoral heterogeneity in primary glioblastoma. Science *344*, 1396–1401. https://doi.org/10.1126/science.1254257.

9. Asp, M., Bergenstråhle, J., and Lundeberg, J. (2020). Spatially resolved transcriptomes-next generation tools for tissue exploration. Bioessays *42*, e1900221. https://doi.org/10.1002/bies.201900221.

10. Moncada, R., Barkley, D., Wagner, F., Chiodin, M., Devlin, J.C., Baron, M., Hajdu, C.H., Simeone, D.M., and Yanai, I. (2020). Integrating microarray-based spatial transcriptomics and single-cell RNA-seq reveals tissue architecture in pancreatic ductal adenocarcinomas. Nat. Biotechnol. *38*, 333–342. https://doi.org/10.1038/s41587-019-0392-8.

11. Ji, A.L., Rubin, A.J., Thrane, K., Jiang, S., Reynolds, D.L., Meyers, R.M., Guo, M.G., George, B.M., Mollbrink, A., Bergenstråhle, J., et al. (2020). Multimodal analysis of composition and spatial architecture in human squamous cell carcinoma. Cell *182*, 497–514.e22. https://doi.org/10.1016/j.cell.2020.05.039.

12. Afify, S.M., and Seno, M. (2019). Conversion of stem cells to cancer stem cells: undercurrent of cancer initiation. Cancers *11*, 345. https://doi.org/10.3390/cancers11030345.

13. Toh, T.B., Lim, J.J., Hooi, L., Rashid, M.B.M.A., and Chow, E.K.H. (2020). Targeting Jak/Stat pathway as a therapeutic strategy against SP/CD44+ tumorigenic cells in Akt/beta-catenin-driven hepatocellular carcinoma. J. Hepatol. *72*, 104–118. https://doi.org/10.1016/j.jhep.2019.08.035.

14. Gu, Y., Wei, X., Sun, Y., Gao, H., Zheng, X., Wong, L.L., Jin, L., Liu, N., Hernandez, B., Peplowska, K., et al. (2019). miR-192-5p silencing by genetic aberrations is a key event in hepatocellular carcinomas with cancer stem cell features. Cancer Res. *79*, 941–953. https://doi.org/10.1158/0008-5472.CAN-18-1675.

15. Lawson, D.A., Bhakta, N.R., Kessenbrock, K., Prummel, K.D., Yu, Y., Takai, K., Zhou, A., Eyob, H., Balakrishnan, S., Wang, C.Y., et al. (2015). Single-cell analysis reveals a stem-cell program in human metastatic breast cancer cells. Nature *526*, 131–135. https://doi.org/10.1038/nature15260.

16. Ho, D.W.H., Tsui, Y.M., Sze, K.M.F., Chan, L.K., Cheung, T.T., Lee, E., Sham, P.C., Tsui, S.K.W., Lee, T.K.W., and Ng, I.O.L. (2019). Single-cell transcriptomics reveals the landscape of intra-tumoral heterogeneity and stemness-related subpopulations in liver cancer. Cancer Lett. *459*, 176–185. https://doi.org/10.1016/j.canlet.2019.06.002.

17. Lambert, A.W., Pattabiraman, D.R., and Weinberg, R.A. (2017). Emerging biological principles of metastasis. Cell *168*, 670–691. https://doi.org/10.1016/j.cell.2016.11.037.

18. Tirosh, I., Venteicher, A.S., Hebert, C., Escalante, L.E., Patel, A.P., Yizhak, K., Fisher, J.M., Rodman, C., Mount, C., Filbin, M.G., et al. (2016). Single-cell RNA-seq supports a developmental hierarchy in human oligodendroglioma. Nature *539*, 309–313. https://doi.org/10.1038/nature20123.

19. Amann, T., Bataille, F., Spruss, T., Mühlbauer, M., Gäbele, E., Schölmerich, J., Kiefer, P., Bosserhoff, A.K., and Hellerbrand, C. (2009). Activated hepatic stellate cells promote tumorigenicity of hepatocellular carcinoma. Cancer Sci. *100*, 646–653. https://doi.org/10.1111/j.1349-7006.2009.01087.x.

20. Velasco-Velázquez, M.A., Yu, Z., Jiao, X., and Pestell, R.G. (2009). Cancer stem cells and the cell cycle: targeting the drive behind breast cancer. Expert Rev. Anticancer Ther. *9*, 275–279. https://doi.org/10.1586/14737140.9.3.275.

21. Xu, Q., Chen, S., Hu, Y., and Huang, W. (2021). Single-cell RNA transcriptome reveals the intra-tumoral heterogeneity and regulators underlying tumor progression in metastatic pancreatic ductal adenocarcinoma. Cell Death Dis. *7*, 331. https://doi.org/10.1038/s41420-021-00663-1.

22. Teschendorff, A.E., and Enver, T. (2017). Single-cell entropy for accurate estimation of differentiation potency from a cell's transcriptome. Nat. Commun. *8*, 15599. https://doi.org/10.1038/ncomms15599.

23. DeTomaso, D., and Yosef, N. (2021). Hotspot identifies informative gene modules across modalities of single-cell genomics. Cell Syst. *12*, 446–456.e9. https://doi.org/10.1016/j.cels.2021.04.005.

24. Kondo, T., Setoguchi, T., and Taga, T. (2004). Persistence of a small subpopulation of cancer stem-like cells in the C6 glioma cell line. Proc. Natl. Acad. Sci. USA *101*, 781–786. https://doi.org/10.1073/pnas.0307618100.

25. Piccirillo, S.G.M., Combi, R., Cajola, L., Patrizi, A., Redaelli, S., Bentivegna, A., Baronchelli, S., Maira, G., Pollo, B., Mangiola, A., et al. (2009). Distinct pools of cancer stem-like cells coexist within human glioblastomas and display different tumorigenicity and

independent genomic evolution. Oncogene *28*, 1807–1811. https://doi.org/10.1038/onc.2009.27.

26. Chen, W., Dong, J., Haiech, J., Kilhoffer, M.C., and Zeniou, M. (2016). Cancer stem cell quiescence and plasticity as major challenges in cancer therapy. Stem Cell. Int. *2016*, 1740936. https://doi.org/10.1155/2016/1740936.

27. Van den Berge, K., Roux de Bézieux, H., Street, K., Saelens, W., Cannoodt, R., Saeys, Y., Dudoit, S., and Clement, L. (2020). Trajectory-based differential expression analysis for single-cell sequencing data. Nat. Commun. *11*, 1201. https://doi.org/10.1038/s41467-020-14766-3.

28. Prasetyanti, P.R., and Medema, J.P. (2017). Intra-tumor heterogeneity from a cancer stem cell perspective. Mol. Cancer *16*, 41. https://doi.org/10.1186/s12943-017-0600-4.

29. Cancer Genome Atlas Research Network, Weinstein, J.N., Collisson, E.A., Mills, G.B., Shaw, K.R.M., Ozenberger, B.A., Ellrott, K., Shmulevich, I., Sander, C., and Stuart, J.M. (2013). The cancer genome atlas pan-cancer analysis project. Nat. Genet. *45*, 1113–1120. https://doi.org/10.1038/ng.2764.

30. Gao, Q., Zhu, H., Dong, L., Shi, W., Chen, R., Song, Z., Huang, C., Li, J., Dong, X., Zhou, Y., et al. (2019). Integrated proteogenomic characterization of HBV-related hepatocellular carcinoma. Cell *179*, 1240. https://doi.org/10.1016/j.cell.2019.10.038.

31. Batlle, E., and Clevers, H. (2017). Cancer stem cells revisited. Nat. Med. *23*, 1124–1134. https://doi.org/10.1038/nm.4409.

32. Gruosso, T., Gigoux, M., Manem, V.S.K., Bertos, N., Zuo, D., Perlitch, I., Saleh, S.M.I., Zhao, H., Souleimanova, M., Johnson, R.M., et al. (2019). Spatially distinct tumor immune microenvironments stratify triple-negative breast cancers. J. Clin. Invest. *129*, 1785–1800. https://doi.org/10.1172/JCI96313.

33. Li, H., van der Leun, A.M., Yofe, I., Lubling, Y., Gelbard-Solodkin, D., van Akkooi, A.C.J., van den Braber, M., Rozeman, E.A., Haanen, J.B.A.G., Blank, C.U., et al. (2019). Dysfunctional CD8 T cells form a proliferative, dynamically regulated compartment within human melanoma. Cell *176*, 775–789.e18. https://doi.org/10.1016/j.cell.2018.11.043.

34. Price, M.J., Patterson, D.G., Scharer, C.D., and Boss, J.M. (2018). Progressive upregulation of oxidative metabolism facilitates plasmablast differentiation to a T-independent antigen. Cell Rep. *23*, 3152–3159. https://doi.org/10.1016/j.celrep.2018.05.053.

35. Zhou, J., Tang, Z., Gao, S., Li, C., Feng, Y., and Zhou, X. (2020). Tumor-associated macrophages: recent insights and therapies. Front. Oncol. *10*, 188. https://doi.org/10.3389/fonc.2020.00188.

36. Wei, C., Yang, C., Wang, S., Shi, D., Zhang, C., Lin, X., Liu, Q., Dou, R., and Xiong, B. (2019). Crosstalk between cancer cells and tumor associated macrophages is required for mesenchymal circulating tumor cell-mediated colorectal cancer metastasis. Mol. Cancer *18*, 64. https://doi.org/10.1186/s12943-019-0976-4.

37. Lawrence, T., and Natoli, G. (2011). Transcriptional regulation of macrophage polarization: enabling diversity with identity. Nat. Rev. Immunol. *11*, 750–761. https://doi.org/10.1038/nri3088.

38. Remmerie, A., and Scott, C.L. (2018). Macrophages and lipid metabolism. Cell. Immunol. *330*, 27–42. https://doi.org/10.1016/j.cellimm.2018.01.020.

39. Efremova, M., Vento-Tormo, M., Teichmann, S.A., and Vento-Tormo, R. (2020). CellPhoneDB: inferring cell-cell communication from combined expression of multi-subunit ligand-receptor complexes. Nat. Protoc. *15*, 1484–1506. https://doi.org/10.1038/s41596-020-0292-x.

40. Strasly, M., Doronzo, G., Cappello, P., Valdembri, D., Arese, M., Mitola, S., Moore, P., Alessandri, G., Giovarelli, M., and Bussolino, F. (2004). CCL16 activates an angiogenic program in vascular endothelial cells. Blood *103*, 40–49. https://doi.org/10.1182/blood-2003-05-1387.

41. Wu, R., Guo, W., Qiu, X., Wang, S., Sui, C., Lian, Q., Wu, J., Shan, Y., Yang, Z., Yang, S., et al. (2021). Comprehensive analysis of spatial architecture in primary liver cancer. Sci. Adv. *7*, eabg3750. https://doi.org/10.1126/sciadv.abg3750.

42. Travelli, C., Colombo, G., Mola, S., Genazzani, A.A., and Porta, C. (2018). NAMPT: a pleiotropic modulator of monocytes and macrophages. Pharmacol. Res. *135*, 25–36. https://doi.org/10.1016/j.phrs.2018.06.022.

43. Clara, J.A., Monge, C., Yang, Y., and Takebe, N. (2020). Targeting signalling pathways and the immune microenvironment of cancer stem cells - a clinical update. Nat. Rev. Clin. Oncol. *17*, 204–232. https://doi.org/10.1038/s41571-019-0293-2.

44. Wang, C., Zhu, X., Feng, W., Yu, Y., Jeong, K., Guo, W., Lu, Y., and Mills, G.B. (2016). Verteporfin inhibits YAP function through up-regulating 14-3-3sigma sequestering YAP in the cytoplasm. Am. J. Cancer Res. *6*, 27–37.

45. Chen, Y.A., Lu, C.Y., Cheng, T.Y., Pan, S.H., Chen, H.F., and Chang, N.S. (2019). WW domain-containing proteins YAP and TAZ in the hippo pathway as key regulators in stemness maintenance, tissue homeostasis, and tumorigenesis. Front. Oncol. *9*, 60. https://doi.org/10.3389/fonc.2019.00060.

46. Weiler, S.M.E., Pinna, F., Wolf, T., Lutz, T., Geldiyev, A., Sticht, C., Knaub, M., Thomann, S., Bissinger, M., Wan, S., et al. (2017). Induction of chromosome instability by activation of yes-associated protein and forkhead box M1 in liver cancer. Gastroenterology *152*, 2037–2051. https://doi.org/10.1053/j.gastro.2017.02.018.

47. Heindl, A., Nawaz, S., and Yuan, Y. (2015). Mapping spatial heterogeneity in the tumor microenvironment: a new era for digital pathology. Lab. Invest. *95*, 377–384. https://doi.org/10.1038/labinvest.2014.155.

48. Bedard, P.L., Hansen, A.R., Ratain, M.J., and Siu, L.L. (2013). Tumour heterogeneity in the clinic. Nature *501*, 355–364. https://doi.org/10.1038/nature12627.

49. Taniguchi, S., Elhance, A., Van Duzer, A., Kumar, S., Leitenberger, J.J., and Oshimori, N. (2020). Tumor-initiating cells establish an IL-33-TGF-beta niche signaling loop to promote cancer progression. Science *369*, eaay1813. https://doi.org/10.1126/science.aay1813.

50. Sun, Y.F., Wu, L., Liu, S.P., Jiang, M.M., Hu, B., Zhou, K.Q., Guo, W., Xu, Y., Zhong, Y., Zhou, X.R., et al. (2021). Dissecting spatial heterogeneity and the immune-evasion mechanism of CTCs by single-cell RNA-seq in hepatocellular carcinoma. Nat. Commun. *12*, 4091. https://doi.org/10.1038/s41467-021-24386-0.

51. Das, B., Tsuchida, R., Malkin, D., Koren, G., Baruchel, S., and Yeger, H. (2008). Hypoxia enhances tumor stemness by increasing the invasive and tumorigenic side population fraction. Stem Cell. *26*, 1818–1830. https://doi.org/10.1634/stemcells.2007-0724.

52. Papale, M., Buccarelli, M., Mollinari, C., Russo, M.A., Pallini, R., Ricci-Vitiani, L., and Tafani, M. (2020). Hypoxia, inflammation and necrosis as determinants of glioblastoma cancer stem cells progression. Int. J. Mol. Sci. *21*, 2660. https://doi.org/10.3390/ijms21082660.

53. Jinushi, M., Chiba, S., Yoshiyama, H., Masutomi, K., Kinoshita, I., Dosaka-Akita, H., Yagita, H., Takaoka, A., and Tahara, H. (2011). Tumor-associated macrophages regulate tumorigenicity and anticancer drug responses of cancer stem/initiating cells. Proc. Natl. Acad. Sci. USA *108*, 12425–12430. https://doi.org/10.1073/pnas.1106645108.

54. Liu, D., Lu, Q., Wang, X., Wang, J., Lu, N., Jiang, Z., Hao, X., Li, J., Liu, J., Cao, P., et al. (2019). LSECtin on tumor-associated macrophages enhances breast cancer stemness via interaction with its receptor BTN3A3. Cell Res. *29*, 365–378. https://doi.org/10.1038/s41422-019-0155-6.

55. Zhang, Q., He, Y., Luo, N., Patel, S.J., Han, Y., Gao, R., Modak, M., Carotta, S., Haslinger, C., Kind, D., et al. (2019). Landscape and dynamics of single immune cells in hepatocellular carcinoma. Cell *179*, 829–845.e20. https://doi.org/10.1016/j.cell.2019.10.003.

56. Imajo, M., Miyatake, K., Iimura, A., Miyamoto, A., and Nishida, E. (2012). A molecular mechanism that links Hippo signalling to the inhibition of Wnt/beta-catenin signalling. EMBO J. *31*, 1109–1122. https://doi.org/10.1038/emboj.2011.487.

57. Meng, Z., Moroishi, T., and Guan, K.L. (2016). Mechanisms of Hippo pathway regulation. Genes Dev. *30*, 1–17. https://doi.org/10.1101/gad.274027.115.

58. Dobin, A., Davis, C.A., Schlesinger, F., Drenkow, J., Zaleski, C., Jha, S., Batut, P.,

Chaisson, M., and Gingeras, T.R. (2013). STAR: ultrafast universal RNA-seq aligner. Bioinformatics *29*, 15–21. https://doi.org/10.1093/bioinformatics/bts635.

59. Satija, R., Farrell, J.A., Gennert, D., Schier, A.F., and Regev, A. (2015). Spatial reconstruction of single-cell gene expression data. Nat. Biotechnol. *33*, 495–502. https://doi.org/10.1038/nbt.3192.

60. Robinson, M.D., McCarthy, D.J., and Smyth, G.K. (2010). edgeR: a Bioconductor package for differential expression analysis of digital gene expression data. Bioinformatics *26*, 139–140. https://doi.org/10.1093/bioinformatics/btp616.

61. Korsunsky, I., Millard, N., Fan, J., Slowikowski, K., Zhang, F., Wei, K., Baglaenko, Y., Brenner, M., Loh, P.R., and Raychaudhuri, S. (2019). Fast, sensitive and accurate integration of single-cell data with Harmony. Nat. Methods *16*, 1289–1296. https://doi.org/10.1038/s41592-019-0619-0.

62. Hänzelmann, S., Castelo, R., and Guinney, J. (2013). GSVA: gene set variation analysis for microarray and RNA-seq data. BMC Bioinf. *14*, 7. https://doi.org/10.1186/1471-2105-14-7.

63. Qiu, X., Hill, A., Packer, J., Lin, D., Ma, Y.A., and Trapnell, C. (2017). Single-cell mRNA quantification and differential analysis with Census. Nat. Methods *14*, 309–315. https://doi.org/10.1038/nmeth.4150.

64. Guo, M., Bao, E.L., Wagner, M., Whitsett, J.A., and Xu, Y. (2017). SLICE: determining cell differentiation and lineage based on single cell entropy. Nucleic Acids Res. *45*, e54. https://doi.org/10.1093/nar/gkw1278.

65. Vento-Tormo, R., Efremova, M., Botting, R.A., Turco, M.Y., Vento-Tormo, M., Meyer, K.B., Park, J.E., Stephenson, E., Polański, K., Goncalves, A., et al. (2018). Single-cell reconstruction of the early maternal-fetal interface in humans. Nature *563*, 347–353. https://doi.org/10.1038/s41586-018-0698-6.

66. Shannon, P., Markiel, A., Ozier, O., Baliga, N.S., Wang, J.T., Ramage, D., Amin, N., Schwikowski, B., and Ideker, T. (2003). Cytoscape: a software environment for integrated models of biomolecular interaction networks. Genome Res. *13*, 2498–2504. https://doi.org/10.1101/gr.1239303.

67. Wu, F., Fan, J., He, Y., Xiong, A., Yu, J., Li, Y., Zhang, Y., Zhao, W., Zhou, F., Li, W., et al. (2021). Single-cell profiling of tumor heterogeneity and the microenvironment in advanced non-small cell lung cancer. Nat. Commun. *12*, 2540. https://doi.org/10.1038/s41467-021-22801-0.

68. Zhao, X., Wu, S., Fang, N., Sun, X., and Fan, J. (2020). Evaluation of single-cell classifiers for single-cell RNA sequencing data sets. Briefings Bioinf. *21*, 1581–1595. https://doi.org/10.1093/bib/bbz096.

69. Macosko, E.Z., Basu, A., Satija, R., Nemesh, J., Shekhar, K., Goldman, M., Tirosh, I., Bialas, A.R., Kamitaki, N., Martersteck, E.M., et al. (2015). Highly parallel genome-wide expression profiling of individual cells using nanoliter droplets. Cell *161*, 1202–1214. https://doi.org/10.1016/j.cell.2015.05.002.

70. Stuart, T., Butler, A., Hoffman, P., Hafemeister, C., Papalexi, E., Mauck, W.M., 3rd, Hao, Y., Stoeckius, M., Smibert, P., and Satija, R. (2019). Comprehensive integration of single-cell data. Cell *177*, 1888–1902.e21. https://doi.org/10.1016/j.cell.2019.05.031.

71. Azizi, E., Carr, A.J., Plitas, G., Cornish, A.E., Konopacki, C., Prabhakaran, S., Nainys, J., Wu, K., Kiseliovas, V., Setty, M., et al. (2018). Single-cell map of diverse immune phenotypes in the breast tumor microenvironment. Cell *174*, 1293–1308.e36. https://doi.org/10.1016/j.cell.2018.05.060.

72. Tang-Huau, T.L., Gueguen, P., Goudot, C., Durand, M., Bohec, M., Baulande, S., Pasquier, B., Amigorena, S., and Segura, E. (2018). Human in vivo-generated monocyte-derived dendritic cells and macrophages cross-present antigens through a vacuolar pathway. Nat. Commun. *9*, 2570. https://doi.org/10.1038/s41467-018-04985-0.

73. Jin, S., Li, R., Chen, M.Y., Yu, C., Tang, L.Q., Liu, Y.M., Li, J.P., Liu, Y.N., Luo, Y.L., Zhao, Y., et al. (2020). Single-cell transcriptomic analysis defines the interplay between tumor cells, viral infection, and the microenvironment in nasopharyngeal carcinoma. Cell Res. *30*, 950–965. https://doi.org/10.1038/s41422-020-00402-8.

74. Vieira Braga, F.A., Kar, G., Berg, M., Carpaij, O.A., Polanski, K., Simon, L.M., Brouwer, S., Gomes, T., Hesse, L., Jiang, J., et al. (2019). A cellular census of human lungs identifies novel cell states in health and in asthma. Nat. Med. *25*, 1153–1163. https://doi.org/10.1038/s41591-019-0468-5.

75. Yu, G., Wang, L.G., Han, Y., and He, Q.Y. (2012). clusterProfiler: an R package for comparing biological themes among gene clusters. OMICS *16*, 284–287. https://doi.org/10.1089/omi.2011.0118.

76. Subramanian, A., Tamayo, P., Mootha, V.K., Mukherjee, S., Ebert, B.L., Gillette, M.A., Paulovich, A., Pomeroy, S.L., Golub, T.R., Lander, E.S., and Mesirov, J.P. (2005). Gene set enrichment analysis: a knowledge-based approach for interpreting genome-wide expression profiles. Proc. Natl. Acad. Sci. USA *102*, 15545–15550. https://doi.org/10.1073/pnas.0506580102.

77. Kurtenbach, S., Cruz, A.M., Rodriguez, D.A., Durante, M.A., and Harbour, J.W. (2021). Uphyloplot2: visualizing phylogenetic trees from single-cell RNA-seq data. BMC Genom. *22*, 419. https://doi.org/10.1186/s12864-021-07739-3.

78. Stewart, C.A., Gay, C.M., Xi, Y., Sivajothi, S., Sivakamasundari, V., Fujimoto, J., Bolisetty, M., Hartsfield, P.M., Balasubramaniyan, V., Chalishazar, M.D., et al. (2020). Single-cell analyses reveal increased intratumoral heterogeneity after the onset of therapy resistance in small-cell lung cancer. Nat. Can. (Ott.) *1*, 423–436. https://doi.org/10.1038/s43018-019-0020-z.

79. Pope, S.D., and Medzhitov, R. (2018). Emerging principles of gene expression programs and their regulation. Mol. Cell *71*, 389–397. https://doi.org/10.1016/j.molcel.2018.07.017.

80. Kotliar, D., Veres, A., Nagy, M.A., Tabrizi, S., Hodis, E., Melton, D.A., and Sabeti, P.C. (2019). Identifying gene expression programs of cell-type identity and cellular activity with single-cell RNA-Seq. Elife *8*, e43803. https://doi.org/10.7554/eLife.43803.

81. Lin, Y., Peng, L., Dong, L., Liu, D., Ma, J., Lin, J., Chen, X., Lin, P., Song, G., Zhang, M., et al. (2022). Geospatial immune heterogeneity reflects the diverse tumor-immune interactions in intrahepatic cholangiocarcinoma. Cancer Discov. *12*, 2350–2371. https://doi.org/10.1158/2159-8290.CD-21-1640.

82. Li, H., Jiang, Y., Hu, J., Xu, J., Chen, L., Zhang, G., Zhao, J., Zong, S., Guo, Z., Li, X., et al. (2023). The U2AF65/circNCAPG/RREB1 feedback loop promotes malignant phenotypes of glioma stem cells through activating the TGF-beta pathway. Cell Death Dis. *14*, 23. https://doi.org/10.1038/s41419-023-05556-y.

83. Larionova, T.D., Bastola, S., Aksinina, T.E., Anufrieva, K.S., Wang, J., Shender, V.O., Andreev, D.E., Kovalenko, T.F., Arapidi, G.P., Shnaider, P.V., et al. (2022). Alternative RNA splicing modulates ribosomal composition and determines the spatial phenotype of glioblastoma cells. Nat. Cell Biol. *24*, 1541–1557. https://doi.org/10.1038/s41556-022-00994-w.

84. Hu, Y., and Smyth, G.K. (2009). ELDA: extreme limiting dilution analysis for comparing depleted and enriched populations in stem cell and other assays. J. Immunol. Methods *347*, 70–78. https://doi.org/10.1016/j.jim.2009.06.008.

85. Minutti, C.M., Modak, R.V., Macdonald, F., Li, F., Smyth, D.J., Dorward, D.A., Blair, N., Husovsky, C., Muir, A., Giampazolias, E., et al. (2019). A macrophage-pericyte Axis directs tissue restoration via amphiregulin-induced transforming growth factor beta activation. Immunity *50*, 645–654.e6. https://doi.org/10.1016/j.immuni.2019.01.008.

86. Ren, C., Ren, X., Cao, D., Zhao, H., Zhai, Z., Li, H., Li, Y., Fu, X., He, J., and Zhao, H. (2020). CNOT7 depletion reverses natural killer cell resistance by modulating the tumor immune microenvironment of hepatocellular carcinoma. FEBS Open Bio *10*, 847–860. https://doi.org/10.1002/2211-5463.12836.

STAR★METHODS

KEY RESOURCES TABLE

REAGENT or RESOURCE	SOURCE	IDENTIFIER
Antibodies		
Rabbit monoclonal anti-TOP2A	Cell Signaling Technology	Cat#12286; RRID: AB_2797871
Rabbit monoclonal anti-CENPF	Abcam	Cat#ab5; RRID: AB_304721
Rabbit monoclonal anti-β-actin	Boster	Cat#BM0627
Rabbit monoclonal anti-CD168	Abcam	Cat#ab124729; RRID: AB_10975797
Rabbit monoclonal anti-Ki-67	Boster	Cat#M00254-9
Rabbit monoclonal anti-PCNA	Boster	Cat#M00125-3
Rabbit monoclonal anti-YAP1	Abcam	Cat#ab52771; RRID: AB_2219141
Rabbit monoclonal anti-Phospho-YAP1	Cell Signaling Technology	Cat#13008
Rabbit monoclonal anti-TAZ	Abcam	Cat#ab224239
Rabbit monoclonal anti-TEAD4	Abcam	Cat#ab58310
Rabbit monoclonal anti-β-catenin	Boster	Cat#BM0627
Rabbit monoclonal anti-GAPDH	Boster	Cat#A00227-1
Rabbit monoclonal anti-histone-H3	Boster	Cat#A12477-2
Biological samples		
Human HCC samples	Shanxi Bethune Hospital Shanxi Medical University	N/A
Chemicals, peptides, and recombinant proteins		
GEXSCOPE® tissue preservation solution	Singleron Biotechnologies	N/A
GEXSCOPE® tissue dissociation solution	Singleron Biotechnologies	N/A
PBS	Boster	PYG0123
DMEM	Boster	PYG0073
RPMI 1640	Boster	PYG0006
Opti-MEM	Life Technologies	Cat # 31985070
FBS	GIBCO	Cat # 16140071
TriZOl	Invitrogen	Cat # 15596026
Bovine Serum Albumin	Sigma	Cat #B2064
Advanced DMEM/F12	Thermo Fisher Scientific	Cat # 12634010
DNase I	Sigma	Cat# D4527
Critical commercial assays		
Human TGF beta 1 ELISA Kit	abcam	Cat# ab108912
Human TGF-beta1 ELISA Kit	proteintech	Cat # KE00002
BCA protein assay kit	Boster	Cat# AR0146
PrimeScript RT Master kit	YEASEN	Cat# 11214ES60
Mix SYBR Green Master kit	YEASEN	Cat# 11201ES08
Deposited data		
Single-cell transcriptome data of LC033	This paper	GSA-Human: HRA004413
Single-cell transcriptome data of LC034	This paper	GSA-Human: HRA004414
Single-cell transcriptome data of LC038	This paper	GSA-Human: HRA004434
CHCC transcriptome data	Gao et al.[30]	PMID: 31585088

(*Continued on next page*)

Continued

REAGENT or RESOURCE	SOURCE	IDENTIFIER
TCGA-LIHC transcriptome data	Cancer Genome AtlasResearch Network, 2017	PMID: 28622513
Spatial Transcriptomic Data	Wu et al.[41]	PMID: 34919432
Experimental models: Cell lines		
THLE-2	Liver Cancer Institute, Zhongshan Hospital, Fudan University (Shanghai, China)	N/A
SK-EP-1	Liver Cancer Institute, Zhongshan Hospital, Fudan University (Shanghai, China)	N/A
SMMC7721	Liver Cancer Institute, Zhongshan Hospital, Fudan University (Shanghai, China)	N/A
HCCLM3	Liver Cancer Institute, Zhongshan Hospital, Fudan University (Shanghai, China)	N/A
BEL-7404	Liver Cancer Institute, Zhongshan Hospital, Fudan University (Shanghai, China)	N/A
Huh7	Liver Cancer Institute, Zhongshan Hospital, Fudan University (Shanghai, China)	N/A
HepG2	National Collection of Authenticated Cell Cultures	CSTR:19375.09.3101HUMSCSP510
Hep3B2.1-7	National Collection of Authenticated Cell Cultures	CSTR:19375.09.3101HUMSCSP5045
PLC/PRF/5	National Collection of Authenticated Cell Cultures	CSTR:19375.09.3101HUMSCSP5095
THP-1	National Collection of Authenticated Cell Cultures	CSTR:19375.09.3101HUMTCHu57
Experimental models: Organisms/strains		
BALB/c Nude Mice CAnN.Cg-Foxn1nu/Crl	Weitonglihua Biotechnology	Cat #401
Oligonucleotides		
TOP2A Forward TTAATGCTGCGGACAACAAACA	Sangon Biotech	N/A
TOP2A Reverse CGACCACCTGTCACTTTCTTTT	Sangon Biotech	N/A
β-actin Forward TTGCGTTACACCCTTTCTTG	Sangon Biotech	N/A
β-actin Reverse CACCTTCACCGTTCCAGTTT	Sangon Biotech	N/A
YAP1 Forward TAGCCCTGCGTAGCCAGTTA	Sangon Biotech	N/A
YAP1 Reverse TCATGCTTAGTCCACTGTCTGT	Sangon Biotech	N/A
TAZ Forward GATCCTGCCGGAGTCTTTCTT	Sangon Biotech	N/A
TAZ Reverse CACGTCGTAGGACTGCTGG	Sangon Biotech	N/A
TEAD4 Forward GAACGGGGACCCTCCAATG	Sangon Biotech	N/A
TEAD4 Reverse GCGAGCATACTCTGTCTCAAC	Sangon Biotech	N/A
U6 Forward CTCGCTTCGGCAGCACA	Sangon Biotech	N/A
U6 Reverse AACGCTTCACGAATTTGCGT	Sangon Biotech	N/A
ACTB Forward GAGAAAATCTGGCACCACACC	Sangon Biotech	N/A
ACTB Reverse GGATAGCACAGCCTGGATAGCAA	Sangon Biotech	N/A
Recombinant DNA		
TOP2A sgRNA	addgene	#138190
Software and algorithms		
CeleScope	www.singleron.bio	https://github.com/singleron-RD/CeleScope
STAR 2.7.10b	Dobin et al.[58]	https://github.com/alexdobin/STAR

(*Continued on next page*)

Continued

REAGENT or RESOURCE	SOURCE	IDENTIFIER
Seurat v3.2.3	Satija et al.[59]	https://github.com/satijalab/seurat
edgeR	Robinson et al.[60]	https://bioconductor.org/packages/release/bioc/html/edgeR.html
Harnomy	Korsunsky et al.[61]	https://github.com/immunogenomics/harmony
GSVA	Hänzelmann et al.[62]	http://www.bioconductor.org/packages/release/bioc/html/GSVA.html
Monocle2	Qiu et al.[63]	http://cole-trapnell-lab.github.io/monocle-release/docs/
SLICE	Guo et al.[64]	http://research.cchmc.org/pbge/slice.html
InferCNV v0.99.0	Tirosh et al.[18]	https://github.com/broadinstitute/infercnv
Cellphone DB v2.1.0	Vento-Tormo et al.[65]	https://github.com/Teichlab/cellphonedb
Cytoscape	Shannon et al.[66]	https://cytoscape.org/

RESOURCE AVAILABILITY

Lead contact

Further information and requests for resources and reagents should be directed to and will be fulfilled by the lead contact, Haoliang Zhao (haoliangzhao@hotmail.com).

Materials availability

This study did not generate new unique reagents.

Data and code availability

- The raw sequence data reported in this paper have been deposited in the Genome Sequence Archive (Genomics, Proteomics & Bioinformatics 2021) in National Genomics Data Center (Nucleic Acids Res 2022), China National Center for Bioinformation/Beijing Institute of Genomics, Chinese Academy of Sciences (GSA-Human: HRA004413, HRA004414, and HRA004434) that are publicly accessible at https://ngdc.cncb.ac.cn/gsa-human.
- The paper does not report original code.
- Any additional information required to reanalyze the data reported in this paper is available from the lead contact upon request.

EXPERIMENTAL MODEL AND SUBJECT DETAILS

Human subject

Liver cancer patients who were pathologically diagnosed with hepatocellular carcinoma at Shanxi Bethune Hospital Shanxi Medical University were enrolled in this study. All patients were treatment naïve, and their clinical characteristics are summarized in Supplementary information, Table S1. Fresh tumors (point A is the center of the tumor: the intersection of the long and short diameters of the tumor cross-section; point C is the tumor edge: the intersection of the long diameter and the edge of the tumor; point B is the non-central sample point in the tumor: the midpoint of the line between point A and point C) and adjacent normal tissue samples (point D is within 2cm from the edge of the tumor; point E is at least 2 cm from matched tumor tissues) were collected as the sample included in this study. Patients or their families signed informed consent. This study was approved by the Institutional Review Board (IRB) of the Shanxi Bethune Hospital (No. YXLL-2019-83). All patients gave informed consent for the collection of clinical information, tissue collection, and research testing.

Cell lines

Cell lines (HepG2, Hep3B2.1-7, PLC/PRF/5, and THP-1) were purchased from the Shanghai Cell Bank, Chinese Academy of Sciences. Human liver cancer cell lines (THLE-2, SK-EP-1, SMMC7721, HCCLM3, BEL-7404, and Huh7) were obtained from the Liver Cancer Institute, Zhongshan Hospital, Fudan University

(Shanghai, China). All cell lines used in this study were characterized by the cell bank based on cell morphology, post-freeze viability, isoenzyme analysis, DNA fingerprinting analysis, mycoplasma contamination testing, and bacterial and fungal contamination. HCC cell lines were cultured in Dulbecco's modified Eagle's medium (DMEM) containing 10% fetal bovine serum (FBS) supplemented with 100 IU/ml penicillin and 100 μg/ml streptomycin, and incubated at 37 C under a humidified atmosphere with 5% CO_2.THP-1 were cultured in 1640 containing 10% FBS. The cells were transfected with 100nM of si-*Ctrl* (SIGS0002902-4, Ribobio Co. Guangzhou, China) or si-*TOP2A* (SIGS0002902-4, Ribobio Co. Guangzhou, China) using Lipofectamine® 3000 transfection reagent (ThermoFisher Scientific, Waltham, MA) accordance with the product instructions.

Animals

Nude mice (four weeks old, female) were purchased from The Weitonglihua Biotechnology (Beijing, China). Nude mice were housed in sterile cages (constant temperature and humidity, SPF level) according to the institutional guidelines for animal care. All animals were treated humanely in accordance with the Guide for the Care and Use of Laboratory Animals prepared by the National Academy of Sciences and the National Institutes of Health (NIH publication 86-23, revised 1985). This animal experiment was approved by the Ethics Committee of Shanxi Bethune Hospital (No: SBQLL-2020-038).

METHOD DETAILS

Single-cell isolation

Fresh tumor and adjacent normal tissue samples were surgically removed from patients and immersed in a complete medium containing 90% Dulbecco's modified eagle medium (DMEM; Cat#11054001, GIBCO) and 10% fetal bovine serum (FBS; Cat#16140071, GIBCO). Cut into suitable small pieces (1-3mm in diameter) , and wash 3 times with Hanks Balanced Salt Solution (HBSS). Subsequently, the samples were immediately stored in the GEXSCOPE® tissue preservation solution (Singleron Biotechnologies, Nanjing, China) at a temperature of 4 °C. It was then digested in 2 ml GEXSCOPE® tissue dissociation solution (Singleron Biotechnologies) in a petri dish according to the manufacturer's instructions. In short, the sample is gently digested on a shaker at 37°C for 15 minutes and then filtered through a 40-micron sterile filter (Corning). The cells were then centrifuged at 300 × g 4 °C for 5 minutes, and the cell pellet was resuspended in 1 ml PBS (HyClone). Next, use trypan blue staining with a hemocytometer to count the cell suspension and evaluate its viability (TC20 automatic cell counter, Bio-Rad). During the dissociation process, keep the sample on ice as much as possible, and the whole process is completed in <90 minutes. The above steps refer to Singleron Biotechnologies standard process.[67]

Single-cell RNA sequencing library preparation

The concentration of single-cell suspension was adjusted to 1 × 10^5 cells/mL in PBS (HyClone). Single-cell suspensions were then loaded onto microfluidic devices and scRNA-seq libraries were constructed according to Singleron GEXSCOPE® protocol by GEXSCOPE® Single-Cell RNA Library Kit (Singleron Biotechnologies).[68] Individual libraries were diluted to 4nM and pooled for sequencing. Pools were sequenced on Illumina NovaSeq with 150 bp paired end reads.

Generation of single-cell gene expression matrices

Raw reads were processed to generate gene expression matrices by CeleScope (https://github.com/singleron-RD/CeleScope). Firstly, read_1 without poly_T tails were filtered, then cell barcodes and unique molecular identifiers (UMI) were extracted. Adapters and polyA tails were trimmed before aligning read_2 to GRCh38 (ensemble version 92 annotation) using STAR. Secondly, reads with the same cell barcode, UMI, and gene were grouped together to count the number of UMIs per gene per cell. Cell number was then determined based on the 'knee' method.

Quality control, dimension-reduction, and clustering

Cells were filtered by gene counts between 200 to 5,000 and UMI counts below 30,000. Cells with over 20% mitochondrial content were removed. After filtering, HCC cells were retained for the downstream analyses, with on average 1392 genes and 4452 UMIs per cell. We used functions from Seurat v3.2.3[59] for dimension-reduction and clustering. All gene expression was normalized and scaled using NormalizeData() and ScaleData(). Top 2000 variable genes were selected by FindVariableFeautres() for PCA analysis. Following gene expression normalization, we applied principal component analysis (PCA) to evaluate variably

expressed genes and subsequently used a graph-based clustering method[69,70] to classify the cells into coherent transcriptional clusters. Cells were separated into 42 clusters by FindClusters(), using the top 20 principle components and resolution parameter at 1.2. For subclustering of Lymphocytes, Epithelial_cells, we set the resolution at 1.0. For subclustering of cancer cells, we set the resolution at 1.2. tSNE algorithm was applied to visualize cells in a two-dimensional space.

Differential expression analysis

Differential expression gene (DEG) analyses in pairs were performed with an edgeR algorithm[60] or Wilcoxon signed-rank tests. Genes expressed in more than 10% of the cells in a cluster and with average log (Fold Change) of greater than 0.25 were selected as DEGs by Seurat v3.2.3 FindMarkers() based on Wilcox likelihood-ratio test with default parameters.

Celltype annotation

The cell type identity of each cluster was manually annotated with the expression of canonical markers found in the DEGs combined with knowledge from literatures[71–74] Heatmaps, dot plots, and violin plots displaying the expression of markers used to identify each cell type were generated by Seurat v3.2.3 DoHeatmap()/DotPlot()/Vlnplot().

Batch effect removal

Batch effect between samples was removed by Harnomy.[61] We batched the Myeloid clustering results, as well as the Macrophages and KC subpopulations.

Pathway enrichment analysis

To investigate the potential function of tumor stemness-related genes, the Gene Ontology (GO) and Kyoto Encyclopedia of Genes and Genomes (KEGG) analysis were used with the "clusterProfiler" R package v4.0.2.[75] Pathways with p_adj value less than 0.05 were considered as significantly enriched. For GSVA pathway enrichment analysis, the average gene expression of each cell type was used as input data using the GSVA package.[62] Gene Ontology gene sets including molecular function (MF), biological process (BP), and cellular component (CC) categories were used as reference.[76]

Trajectory analysis

To map differentiation/conversion of cell subtypes in liver cancer microenvironment, pseudotime trajectory analysis was performed with Monocle2.[63] For constructing the trajectory, top 2000 highly variable genes were selected by Seurat v3.2.3 FindVairableFeatures(), and dimension-reduction was performed by DDRTree(). The trajectory was visualized by plot_cell_trajectory().

Single-cell entropy analysis

SLICE (version 0.99.0)[64] was used to evaluate the stemness of cells by the entropy of gene expression based on single-cell expression profiles. After removing ERCC spike-ins and ribosomal genes, a SLICE object was created to perform bootstrap calculation of single-cell gene entropy values by getEntropy() function.

scRNA-seq based CNA detection

The InferCNV package[6] was used to detect the CNAs in malignant cells. As described in InferCNV, we used immune cells as baselines to estimate the CNA of malignant cells. Genes expressed in more than 20 cells were sorted based on their loci on each chromosome. The relative expression values were centered to 1, using 1.5 standard deviation from the residual-normalized expression values as the ceiling. A slide window size of 101 genes was used to smoothen the relative expression on each chromosome, to remove the effect of gene-specific expression. Uphyloplot2[77] taked input from InferCNV to generate evolutionary graphs.

Intra-tumoral heterogeneity (ITH) score calculation

The ITH score was calculated by the algorithm described.[78] The ITH score was defined as the average Euclidean distance between the individual cells and all other cells, in terms of the first 20 principal components derived from the normalized expression levels of highly variable genes. The highly variable gene was identified using the FindVariableFeatures () function in the Seurat package, with default parameters.

Expression programs analysis

The transcriptional programs were extracted by consensus non-negative matrix factorization (cNMF) algorithm, take the gene of top 50 as the meta-signature, and calculate the score of each program for each cell by meta-signature. The 12 meta-program calculated and hierarchical clusteringed according.[79,80]

Least Absolute Shrinkage and Selection Operator (LASSO)

On the basis of linear regression, by increasing the penalty term (lambda × the absolute value of the slope), the overfitting of the model is reduced and the generalization ability of the model is improved. LASSO regression analysis was then performed with the R package glmnet based on the gene expression and clinical data corresponding to the train group. Finally, the marker genes were determined according to the LASSO regression results, the corresponding regression coefficients of each gene were calculated, and the prognosis effect of the regression fitting results (risk score) was verified by Survival and ROC analysis.

Cell-cell interaction analysis

Cell-cell interaction (CCI) between different cell types were predicted based on known ligand–receptor pairs by Cellphone DB v2.1.0.[39] Permutation number for calculating the null distribution of average ligand-receptor pair expression in randomized cell identities was set to 1000. Individual ligand or receptor expression was thresholded by a cutoff based on the average log gene expression distribution for all genes across each cell type. Predicted interaction pairs with p value <0.05 and of average log expression >0.1 were considered as significant. The interaction between cells is visualized by Cytoscape.[66]

Immunohistochemistry (IHC) and multicolor immunofluorescence

The tumor tissue was initially fixed with 4% paraformaldehyde, embedded in paraffin and cut into 5 μm thick sections. The sections were blocked with 10% goat serum and incubated with anti-*TOP2A* (1:200, Cat#12286, CST) or anti-*CENPF* (1:200, Cat#ab224813, Abcam), or anti-ki-67 (1:200, M00254-9, Boster) antibodies at 4°Cat night. After washing with PBS, the sections were incubated with a secondary antibody conjugated with anti-mouse or rabbit horseradish peroxidase at room temperature for 1 hour. Paraffin sections were stained with DAB and hematoxylin. The IHC section slides were observed by a microscope (Nikon, Japan). Multiplexed immunofluorescence was performed as we previously described.[81] Opal-520, Opal-620 (PerkinElmer) and 4′,6-diamidino-2-phenylindole (DAPI) were applied to each antibody for visualization.

Cell counting Kit-8 (CCK-8) assay

The activity of HCC cells was tested by the CCK-8 assay kit (Boster, Wuhan, China). The cells (2×10^3/100μl) were seeded in a 96-well plate and incubated with 5% CO_2 at 37 °C. The CCK-8 stock solution were diluted (1:9) with fresh DMEM to the working mixture. The original medium in the 96 well plate was aspirated off, 100 μL of the CCK-8 mixture was added to each well and incubated at 37 °C for 2 h. The absorbance was measured by a microplate reader (Thermo Fisher Scientific, Inc., Germany) at 450 nm.

Colony formation

HCC cells were seeded in 6-well plates at a density of 1000 cells/well in 2 mL to produce HCC colony. The cells were kept at 37°C in 5% CO_2 for 14 days, and the medium was changed every 2 days. The colonies were fixed with 70% ethanol, and stained with 0.5% crystal violet. The colony consisting of 50 cells were counted using ImageJ (NIH, Bethesda, MD, USA) software. The experiment was carried out in triplicate.

RNA extraction and quantitative Real-time PCR (qRT-PCR)

The total RNA of cells or tissues were extracted with Trizol reagent (Invitrogen, Carlsbad, CA, USA). We use M5 Sprint qPCR RT kit with gDNA remover (Mei5bio, China) to reverse transcribe mRNA into cDNA. First Strand cDNA Synthesis of miRNA TransScript SuperMix (TransGen Biotech, China) was used for the synthesis of miRNA cDNA. qRT-PCR was performed using SYBR premix EX Taq II (Takara, Tokyo, Japan). Reactions were performed on a 7500 Fast Real-Time PCR System (Applied Biosystems, Foster City, CA, USA). ATCB was used as a control for standardizing mRNA.

Isolation of nuclear and cytoplasmic fractions

Cytoplasmic and nuclear fractions of HCC cells were performed by using Subcellular structure separation kit (Boster, Wuhan, China). HCC cells were lysed in a lysis buffer containing protease inhibitors for 10 minutes on ice. HCC cells were lysed in a lysis buffer containing protease inhibitors for 10 minutes on ice. The sediment was washed with PBS for two times, and added protein lysis reagent. nuclear fraction was in the upper layer after centrifugation at 12,000×g for 10 min.

Western blot analysis

The protein was extracted from cells using RIPA lysis buffer (Boster, Wuhan, China) and BCA kit (Boster, Wuhan, China) for quantification. The protein samples were mixed with a loading buffer (BOSTER) at a ratio of 5:1 and subjected to heat. After sodium dodecyl sulfate polyacrylamide gel electrophoresis (SDS-PAGE), the proteins in the gels were transferred onto the polyvinylidene fluoride membrane. The membrane was blocked with 5% non-fit milk powder at room temperature for 2 hours and incubated with the primary antibodies. Next, the proteins were incubated with primary antibodies and the primary antibodies used for analysis were as follows: rabbit anti-TOP2A (1:2,500; Cat#12286, CST), rabbit anti-CENPF (1:200, Cat#ab224813, Abcam), rabbit anti-β-actin (1:10,000; Cat#BM0627, Boster), rabbit anti-Ki-67 (1:2,000; Boster, M00254-9), rabbit anti-PCNA (1:2,000;Boster, M00125-3), rabbit anti-Cyclin A1 (1:1,000;abcam ab53699), rabbit anti-Cyclin B1 (1:2,000;abcam, ab181593), rabbit anti-Cyclin B2 (1:1,000; abcam, ab185622), rabbit anti-Cyclin D1 (1:200; abcam, ab16663), rabbit anti-Cyclin E1 (1:1,000;abcam, abab33911), rabbit anti-YAP1 (1:5,000;abcam, ab52771), rabbit anti-Phospho-YAP1 (1:1,000;CST, 13008), rabbit anti-TAZ (1:500;abcam ab224239), rabbit anti-TEAD4 (1:1,000;abcam ab58310), rabbit anti-GAPDH (1:2,000;Boster A00227-1), and rabbit anti-histone-H3 (1:1,000;Boster A12477-2). The secondary antibodies (1:10,000) was from Proteintech, Wuhan, China. The experiments were repeated three times. Finally, the amplified chemiluminescent system is used to visually detect the signal.

Cancer cells stemness test

HCC tumor stemness is detected by tumor spheroid formation rate. HCC was cultured in DMEM/F12 serum-free medium, and additional: penicillin 100 IU/ml, streptomycin 100 μg/ml, human recombinant epidermal growth factor 20 ng/ml, recombinant basic fibroblast growth factor 20 ng/ml, 1% non-essential amino acids, 1% GlutaMax, 2% B27 supplements, 1% methylcellulose to form a serum-free medium for spheroid culture. Cells are cultured in ultra-low adsorption petri dishes. Sphere formation efficiency (SFE) = the number of cell spheroids with a diameter greater than 75um in each well/the total number of original seeded cells in each well.

Limiting dilution neurosphere formation assays

The Limiting dilution neurosphere formation assays were performed as previous description.[82,83] Briefly, GSCs from dissociated neurospheres were plated into 96-well plates at a density of 1, 3, 6, 12, 25, 50, 100, 200, 400, or 800 cells/well and cultured for 7 days. The data were analysed using Extreme Limiting Dilution Analysis software (https://bioinf.wehi.edu.au/software/elda/index.html).[84]

Primary macrophage extraction

Tumor and liver tissue were cut into small pieces and digested as described above.[85] Tissue were washed in PBS and filtered over a 40 μm nylon mesh and labelled with anti-human CD14 MACS beads. Human *CD14*$^{+}$ monocytes were sorted from cells using EasySep Human CD14 Selection Kit (Stemcell Technology, Cambridge, Massachusetts), according to the manufacturer's instructions. *CD14*$^{+}$ cells were purified by magnetic cell sorting (purity was >90%). Those cells were seeded in 12-well tissue culture plates for further experiments.

Co-culture

THP-1 cells were seeded into 6-well plates at a density of 1×10^{6}/mL. PMA (200nmol/L) was added to PRMI1640 medium, which became undifferentiated macrophages (M0) after 24 hours of induction. Then, under the condition that PMA continues to exist, respectively pass: a. Incubate with IFN-γ (20 ng/mL) and LPS (100 ng/mL) for more than 48 hours to polarize M1 macrophages. b. Give IL-4 (20 ng/mL) and IL-13 (20 ng/mL) for more than 48 hours to polarize M2 type macrophages. After the polarization was completed, the cells were resuspended in serum-free RPMI1640 without stimulus, and inoculated into the Transwell chamber at 3×10^{5}/mL. Outside the small room, SK-HEP-1 (low expression of *TOP2A* and

CENPF) was inoculated according to 5×10^4. After the two kinds of cells were co-cultured for 48 hours, HCC cells were collected for subsequent experiments. The co-cultivation process of primary macrophages and tumor cells is basically the same as above. A Transwell (0.4 μm, Corning) was used for co-culture experiments.

Enzyme-linked immunosorbent assay (ELISA)

ELISA was performed as as described above.[86] In this study, the supernatant of tumor cells after co-culture was used for the determination of CXCL12 and TGF-β1. The testing process was carried out in full accordance with the product instructions.

Cell cycle assay

HCC Cells were transfected with siRNA or plasmid for 48 h. Approximately, one million cells were harvested and fixed with 75% ethanol at 20°C overnight. The cells were stained with propidium iodide buffer (BD, NJ) at 37 °C for 30min. The cell cycle was analyzed by a FACSCalibur flow cytometer (Becton Dickinson).

Detection of apoptosis by Annexin V-APC/7-AAD double-staining

HCC cells were washed twice with PBS, digested with 0.25% trypsin for 5 min and centrifuged at 1,000 ×g for 5minat 4°C to collect 5×10^5 cells. The harvested cells then resuspended in 500 μl binding buffer (Boster, Wuhan). 5 μl Annexin V-APC was mixed to the cell suspension, followed by mixing, and then 5 μl 7-AAD was mixed. The samples were incubated at room temperature in the dark for 5-15 min. The apoptosis was detected by using a BD LSRII flow cytometer (BD Biosciences, New Jersey, U.S.). The data were analyzed and graphed using CellQuest Pro (BD Biosciences, New Jersey, U.S.).

Coimmunoprecipitation (co-IP)

The lysate was added to the cell culture plate for full cell lysis at 4 °C. The lysates were centrifuged at 12,000 rpm for 10 min, and the supernatant was collected subsequently. A small amount of lysate was collected and used for other experiments, and the corresponding antibody (10 μg) was added to the remaining lysate, which was incubated overnight at 4 °C. PierceTM Protein A/G Agarose Beads (Thermo Fisher Scientific, Inc.) were washed repeatedly with the lysis buffer. The pretreated beads were added to the cell lysate and incubated for overnight at 4°C, and centrifuged at 2, 500 rpm for 3minat 4 °C. The supernatant was removed, and the agarose beads were washed three times with 1 ml of lysis buffer. Then, 100 μl of 2×SDS loading buffer was added, and samples were incubated at 95 °C for 5 min and subjected to WB analysis.

Tumor xenograft model

To establish human HCC xenograft model in nude mice, HCC cells (5×10^6 cells in 200 μl stably transfected with sh-*Ctrl* and sh-*TOP2A*, Genepharma, Shanghai, China) were injected into the flanks of 4-week-old female athymic nude mice. Tumor volume was measured and recorded every 3 days using the following formula: volume (mm^3) = length (mm) ×width^2 (mm^2)/2. After 24 days, the mice were sacrificed, and the tumors were weighed.

QUANTIFICATION AND STATISTICAL ANALYSIS

Statistical analysis

Data was analyzed was done with GraphPad Prism 5 software (GraphPad Software, Inc., San Diego, CA, USA). The Student's *t*-test was used to analyze the statistical significance between two groups. One-way ANOVA followed by Tukey test was used to perform a comparison among multiple groups. Survival analyses were conducted using log-rank tests. *p*-value less than 0.05 was considered significant. ***$p<0.001$, **$p<0.01$, *$p<0.05$.